Experimental and Analytical Study of the High-Strain Rate Flexural Behavior of SFRC

Mohammad Bakhshi, Ph.D.[1]; Isabel B. Valente[2]; Honeyeh Ramezansefat[3]; Joaquim A. O. Barros[4]; Eduardo N. B. Pereira[5]; and Nuno R. M. Peixinho[6]

Abstract: Steel fiber-reinforced concrete (SFRC) with hooked-end steel fibers was created for use in urban furniture to protect against blast and impact loads. Due to the variety of impact loads that these structures may experience, it is necessary to assess the impact of high strain rates on the flexural behavior of SFRC. This study involved testing SFRC beams with 1% volume content of hooked-end fibers, which were 30 mm long and had an aspect ratio of 80. The beams were tested at different strain rates and in a three-point loading configuration. Four strain rates were tested, ranging from 10^{-6} to 10^{-2} s^{-1}, and impact tests were conducted using a drop weight impact test machine and varying drop heights, corresponding to strain rates ranging from 1 to 20 s^{-1}. Two load cells were used to measure the total impact force and one reaction force, which were then used to assess the inertial force. Two accelerometers measured the maximum acceleration at the midspan of the beams. The results included quasi-static and dynamic load-deflection relationships, dynamic flexural tensile strength, and failure mode of SFRC specimens, as well as the relationship between the inertial force and strain rate. The study revealed that deflection capacity and flexural tensile strength increased with loading rate. The study also provides dynamic to static property ratios, such as flexural tensile strength and fracture energy, which are compared with those recommended by the CEB-FIP Model Code and other researchers. **DOI: 10.1061/JMCEE7.MTENG-16559.**

Author keywords: Drop weight test; Steel fiber-reinforced concrete (SFRC); Flexural behavior; Strain rate; Impact load; Fracture energy.

Introduction

Concrete structures, including highways, buildings, and barriers, are susceptible to dynamic and impact loads over their lifespan, such as vehicle collisions and terrorist attacks. Since concrete is a brittle material, incorporating ductile reinforcements improves the energy dissipation capacity and resistance of concrete structures to dynamic loads (Zhang et al. 2014). Concrete reinforcement with steel fibers is a way to increase the concrete post-cracking strength and energy absorption (Barros and Figueiras 1999; Bentur and Mindess 2006; Yoo et al. 2015). SFRC has been used in several engineering applications since it can decrease, or even eliminate, conventional steel reinforcements with technical and economic advantages (ACI 2017; Zhang et al. 2017). By bridging the cracks in their initiation phase, steel fibers offer resistance to the crack opening process, limiting the maximum crack width to acceptable values regarding serviceability limit state design conditions (Taheri et al. 2020), with a favorable impact on the durability of a concrete structure (Jin et al. 2018). In applications of SFRC with a considerable probability of being subjected to impact load, the SFRC is predominantly subjected to bending moments, such as in the case of slabs supported on soil (Sorelli et al. 2006), columns (Xu et al. 2017), and piles (Ozden and Akdag 2009). Therefore, it is important to evaluate the performance of SFRC structural components under flexural impact loading.

For SFRC, there is no established relationship between strain rate values and mechanical properties, such as compressive strength, tensile strength, or flexural strength. There are two main reasons for this: to measure the dynamic properties of concrete materials, such as tensile strength or fracture energy, which is required for special load equipment, monitoring data acquisition, and test setup (Bakhshi et al. 2023; Lok and Zhao 2004; Zanuy and Ulzurrún 2017; Zhang et al. 2017); and several parameters can influence this phenomenon, such as the SFRC mix composition, geometry, orientation, and distribution of steel fibers (Abaza and Hussein 2016) and dimensions of the tested SFRC element (size effect) (Lok et al. 2002; Ulzurrun and Zanuy 2017). Therefore, the influence of too many variables needs to be assessed to determine the behavior of SFRC under impact loading, erasing the difficulty of obtaining a single formulation that considers the effects of these variables.

In concrete, the impact of strain rate on mechanical properties is typically characterized using the dynamic increase factor (DIF), which is the dynamic to static properties. Many researchers consider that the dynamic tensile behavior of SFRC is well represented by the tensile DIF (Bakhshi et al. 2021; CEB-FIP 1990, 2010; Othman et al. 2019; Zhang et al. 2017, 2014). Some models have been proposed to predict the DIF of concrete tensile strength

[1]Ph.D. Candidate, Dept. of Civil Engineering, Univ. of Minho, Azurem, Guimaraes 4800-058, Portugal (corresponding author). Email: Mohammad.bakhshi.ngd@gmail.com

[2]Assistant Professor, Dept. of Civil Engineering, Univ. of Minho, Azurem, Guimaraes 4800-058, Portugal. ORCID: https://orcid.org/0000-0003-0502-9956. Email: isabelv@civil.uminho.pt

[3]Postdoctoral Researcher, Dept. of Civil Engineering, Univ. of Minho, Azurem, Guimaraes 4800-058, Portugal. Email: honeyrscivil@gmail.com

[4]Full Professor, Dept. of Civil Engineering, Univ. of Minho, Azurem, Guimaraes 4800-058, Portugal. ORCID: https://orcid.org/0000-0003-1528-757X. Email: barros@civil.uminho.pt

[5]Assistant Professor, Dept. of Civil Engineering, Univ. of Minho, Azurem, Guimaraes 4800-058, Portugal. Email: eduardo.pereira@civil.uminho.pt

[6]Assistant Professor, Dept. of Mechanical Engineering, Univ. of Minho, Azurem, Guimaraes 4800-058, Portugal. Email: peixinho@dem.uminho.pt

Note. This manuscript was submitted on March 2, 2023; approved on October 2, 2023; published online on January 27, 2024. Discussion period open until June 27, 2024; separate discussions must be submitted for individual papers. This paper is part of the ***Journal of Materials in Civil Engineering***, © ASCE, ISSN 0899-1561.

(CEB-FIP 1990, 2010; Lok and Zhao 2004; Malvar and Ross 1998; Tran et al. 2016). The one proposed by the CEB-FIP Model Code (CEB-FIP 2010) for determining the dynamic concrete tensile strength is based on the following equation

$$\frac{f_{\text{ctm},dy}}{f_{\text{ctm}}} = \begin{cases} \left(\frac{\dot{\varepsilon}_{ct}}{\dot{\varepsilon}_{ct0}}\right)^{0.018}, & \dot{\varepsilon}_{ct} \le 10 \text{ s}^{-1} \\ 0.0062\left(\frac{\dot{\varepsilon}_{ct}}{\dot{\varepsilon}_{ct0}}\right)^{1/3}, & \dot{\varepsilon}_{ct} > 10 \text{ s}^{-1} \end{cases} \quad (1)$$

where $f_{\text{ctm},dy}$ and f_{ctm} = dynamic and static tensile strength, respectively; $\dot{\varepsilon}_{ct}$ = tensile strain rate (s^{-1}), in the range between 1×10^{-6} and 300 s^{-1}; and $\dot{\varepsilon}_{ct0}$ is the static tensile strain rate, taken as 1×10^{-6} s^{-1}.

Despite the costs and time-consuming aspects, experimental research is still recognized as the most reliable approach to assess concrete properties under impact loading. Furthermore, the obtained results can be used to calibrate key parameters of analytical formulations and assess their predictive performance. Numerous experimental methods have been expanded to study the mechanical characteristics of concrete when subjected to impact loading. Based on the loading rate (strain rate) range, various experimental approaches have been conducted, such as noninstrumented multiple drop weight (Rahmani et al. 2012), weighted pendulum (Charpy) (ACI 2017; Suaris and Shah 1982), instrumented drop weight (Banthia and Mindess 1996), split Hopkinson pressure bar (SPHB) (Lok et al. 2003), and projectile (Wu et al. 2015). Table 1 lists the test methods recommended by Nystrom et al. (Nyström and Gylltoft 2009), according to the strain rate regimes that each one is able to implement.

Ulzurrun and Zanuy (2017) conducted an experiment to investigate the flexural response of SFRC when subjected to impact loading. They utilized a drop weight machine to apply impact loads on unnotched SFRC flexural specimens. The specimens were made with three types of steel fibers (smooth, hooked, and prismatic) and two volumetric contents (0.5% and 1%). Impact loads were applied by dropping a 100 kg mass from heights ranging between 500 and 1,750 mm. DIF values were calculated for both flexural tensile strength and fracture energy, and for all types of SFRCs, the DIF values were found to be greater than one. Since they only performed the drop weight impact test, they did not take into account how the impact testing methodology might have influenced their findings.

Othman et al. (2019) conducted a study on the dynamic flexural behavior of ultrahigh performance SFRC, which has improved static, dynamic, and durability characteristics. They used three different strengths of concrete mixture and three different volume fractions of short steel fibers. The specimens were subjected to quasi-static loadings at three different strain rates (ranging from 10^{-6} to 10^{-4} s^{-1}) and impact loadings with three different impactor heights (150, 300, and 600 mm). Their study found that increasing the fiber volume enhanced the tensile properties and post-peak tensile ductility (the difference between ultimate and peak midspan deflection). However, the effect of inertial force and acceleration during the impact process is a critical aspect that has not been explored, while the effect of the impact test approach was not considered in their study.

Banthia (1987) investigated the strain rate sensitivity of the flexural behavior of SFRC beams. Beams with dimensions of $150 \times 150 \times 1{,}500$ mm^3 were tested under a bending load configuration imposed by a drop weight impact machine at a displacement rate of approximately 4,000 mm/s. The results showed an increase in the peak resisting bending load with strain rate under impact. Similar results were obtained by Zhang et al. (2014) by conducting three-point bending tests on notched beams of SFRC under different displacement rates (from 10^{-3} to 10^{3} mm/s) using a servo-hydraulic machine and a drop weight impact device. The results indicate that the flexural tensile strength and fracture energy of SFRC increased with the displacement rate.

Based on a review of previous experimental studies, the effect of inertial force and acceleration during the impact process as a critical aspect has not been fully explored in previous studies. Additionally, considering the type of test setup as an effective factor in evaluating the strain rate dependency of flexural tensile strength and fracture energy of SFRCs often was overlooked in previous experimental studies. Therefore, it was concluded that experimental research regarding the mechanical behavior of SFRC under impact loadings is still scarce.

The current research aimed to examine the effect of strain rate on the flexural behavior of SFRC with hooked-end fibers. Prismatic specimens with dimensions of $100 \times 100 \times 400$ mm^3 were used, and three-point bending tests were conducted with varying levels of strain rate. Four different strain rates, ranging from 10^{-6} to 10^{-2} s^{-1}, were considered for quasi-static tests, while drop weight impact tests were performed with four different impactor heights (250, 500, 1,000, and 1,500 mm). Impact tests were carried out with a modified instrumented drop weight testing machine at the Laboratory of Mechanical Engineering at the University of Minho. The results were analyzed based on the impact and reaction forces, inertial effect, flexural tensile strength, and fracture energy. The experimental DIF parameters for the flexural tensile strength and fracture energy were calculated and compared with the results obtained using the model recommended by CEB-FIP code and models proposed by other researchers. Finally, the relationship between SFRC fracture energy and strain rate was investigated. A discussion is provided to understand the impact flexural behavior and the influence of the testing methodology and inertial force on the experimental results.

The remaining part of this paper is organized as follows. In section of "Experimental Program," the mix proportion and test setups for SFRC were presented, covering both quasi-static and impact ranges. Three specimens were tested for both the quasi-static range, covering different displacement rates, and the impact range, encompassing various dropping heights. Section of "Test Results and Discussion" examines the various fracture modes and failure patterns observed. Furthermore, to determine the flexural force–deflection diagram and fracture energy values at different strain rates, the parameters of strain rate, midspan deflection, impact, inertia, and reaction forces were delved into in this section. Also, the effects of strain rate and testing approach on the flexural behavior of SFRC were analyzed and discussed, specifically focusing on flexural tensile strength and fracture energy. It also discusses gaps in the existing field of

Table 1. Strain rate regimes and test setup recommended by Nystrom et al. (Nyström and Gylltoft 2009)

Strain rate range (s^{-1})	Regime	Test method
10^{-9}–5×10^{-7}	Creep	Conventional device
5×10^{-7}–5×10^{-2}	Quasi-static	Conventional device
5×10^{-5}–5×10^{-2}	Vehicle impact	Conventional device
10^{-4}–10^{2}	Earthquake	Conventional device; SHPB; drop weight test
5×10^{-2}–5×10^{0}	Plane crash	Drop weight test
10^{-2}–5×10^{4}	Blast	SHPB; drop weight test; Taylor impact
10^{0}–10^{8}	Hard impact	SHPB; drop weight test; Taylor impact; projectile

research to provide additional insight into the outcomes by proposing new models including the influencing factors. Finally, in section of "Conclusions" highlights the concluding remarks.

Experimental Program

Materials Characterization

The mixture used for the SFRC was designed using the volume method recommended by ACI 544 1R (ACI 1996), and consisted of various ingredients, including type I cement 42.5R recommended by BS EN 197-1 (British Standard Euro Norm 2000), Type II fly ash following BS EN 450-1 (British Standard Euro Norm 2012) requirements, fine and coarse aggregates with a maximum size of 12 mm, superplasticizer, hooked-end steel fibers, and water. The proportions of these ingredients are listed in Table 2. According to previous studies (Othman et al. 2019; Othman and Marzouk 2016; Ulzurrun and Zanuy 2017; Wang et al. 2011; Yoo and Banthia 2019; Zanuy and Ulzurrún 2017) and real structural applications of SFRC (Barros et al. 2022a, b), the addition of 1% volume fraction of steel fibers in SFRC provides a good compromise in terms of mechanical performance for the SFRC (flexural, shear and compression) and its cost competitiveness. For hooked end steel fiber volumes greater than 1% in volume, the mix composition should be significantly modified over current practices in the concrete technology in order to efficiently mobilize the fiber reinforcement mechanisms and avoid fiber balling (Tlemat et al. 2003). Furthermore, Banthia and Mindess (1996) found that incorporating a 1% volume fraction of hooked-end steel fibers notably enhances the energy absorption capacity under impact loading. In the current study, the hooked-end steel fibers were added at a volume fraction of 1% and had a density of 7.8 g/cm^3, a length of 30 mm, and an aspect ratio of 80, as shown in Table 3. The water-cement ratio was maintained at 0.3.

Quasi-Static Test

In order to estimate the tensile strength of SFRC beams without the high cost of direct tensile tests, flexural tests are commonly used. To investigate how the tensile strength of SFRC beams varies under different strain rates, three-point notched beam bending tests (3PNBBT) were conducted. The bending tests were performed using a servo-hydraulic testing machine in the quasi-static strain rate range of 10^{-6} to 10^{-2} s^{-1}, with four different displacement rates being selected. Three notched beams ($100 \times 100 \times 400$ mm^3), each with a span of 300 mm, were tested at each strain rate. The notch width was 3 mm, and the notch/beam depth ratio was about 1/6 following the recommendation of the EN 14651 standard and the RILEM TC 162-TDF committee (Vandewalle et al. 2022) with a reduction factor of 1.5. The specimens were rotated 90 degrees with respect to their casting position, to comply with the recommendations of RILEM TC 162-TDF (Vandewalle et al. 2022), assuring that the bottom and top loading surfaces were both smooth. One LVDT was placed at the beam's midspan to measure the deflection. This LVDT was attached to a horizontal steel bar to guarantee the accurate beam's net deflection (see Fig. 1). Another LVDT was installed to measure the crack opening at midspan. A strain gauge was used to measure the strain rate at the midspan compression zone, as depicted in Fig. 1.

In relation to the 3PNBBT, the bending theory of the beam indicates that there is a correlation between the strain rate, denoted by $\dot{\varepsilon}$, at the extreme surfaces of the cross section [the measured strain values are scaled by $50/(50\text{-}8)$ due to small deflections], and the rate of midspan deflection represented by $\dot{\delta}$. This correlation can be determined using the following equation where h, a, and l correspond to the height, notch depth, and span length of the beam, respectively (Othman et al. 2019)

$$\dot{\varepsilon} = \frac{6(h-a)\dot{\delta}}{l^2} \tag{2}$$

Instrumented Drop Weight Impact Test

The drop weight system used in the flexural impact load test is illustrated in Fig. 2. The drop weight system can drop a hammer with a maximum weight of 290 kg from a maximum height of 9 m, corresponding to a theoretical maximum impact velocity of 13.3 m/s. According to the study conducted by Nyström and Gylltoft (2009), the drop weight impact test can apply impact loads at strain rates ranging from 1 to 10^2 (s^{-1}), simulating various impact load scenarios such as earthquakes, blasts, and hard impacts (Table 1). Considering that the mechanical properties of SFRC, such as flexural tensile strength and energy absorption capacity, may vary at different strain rates, four distinct strain rates (impact velocities) were chosen within this range. This selection aims to identify any potential optimizations or limitations in the performance of SFRC under dynamic loading conditions. By exploring these different impact velocities, researchers sought to gain a comprehensive understanding of how SFRC responds to a wide range of real-world impact events. In the study, a 90-kg hammer was dropped from heights of 250, 500, 1,000, and 1,500 mm, corresponding to impact velocities of 2.2, 3.1, 4.4, and 5.4 m/s, respectively. Two load cells capacities of 1,000 and 500 kN, respectively, were used to record the impact force on the top and bottom of the specimen, respectively, at a frequency of 50 samples per millisecond to calculate the inertial force generated in each test.

The compressive strain rate was measured using a strain gauge installed 8 mm below the top surface of the compressive zone, and the measured values were corrected to obtain the strain rate at the top surface. The strain rate was then calculated based on the corrected strain. Two accelerometers were installed at the midspan of

Table 2. Mix proportions of SFRC per m^3

Cement (kg)	Fly ash (kg)	Water-cement content ratio	Fine aggregate (0–4 mm) (kg)	Coarse aggregate (4–12 mm) (kg)	Superplasticizer (kg)	Steel fibers (kg)
400	200	0.3	942	628	4.8	75.8

Table 3. Characteristics and quantity of the steel fibers

Mass (kg/m^3)	Volume (%)	Length (mm)	Diameter (mm)	L/D	Tensile strength (MPa)	Modulus of elasticity (GPa)
75.8	1	30	0.38	80	2,300	210

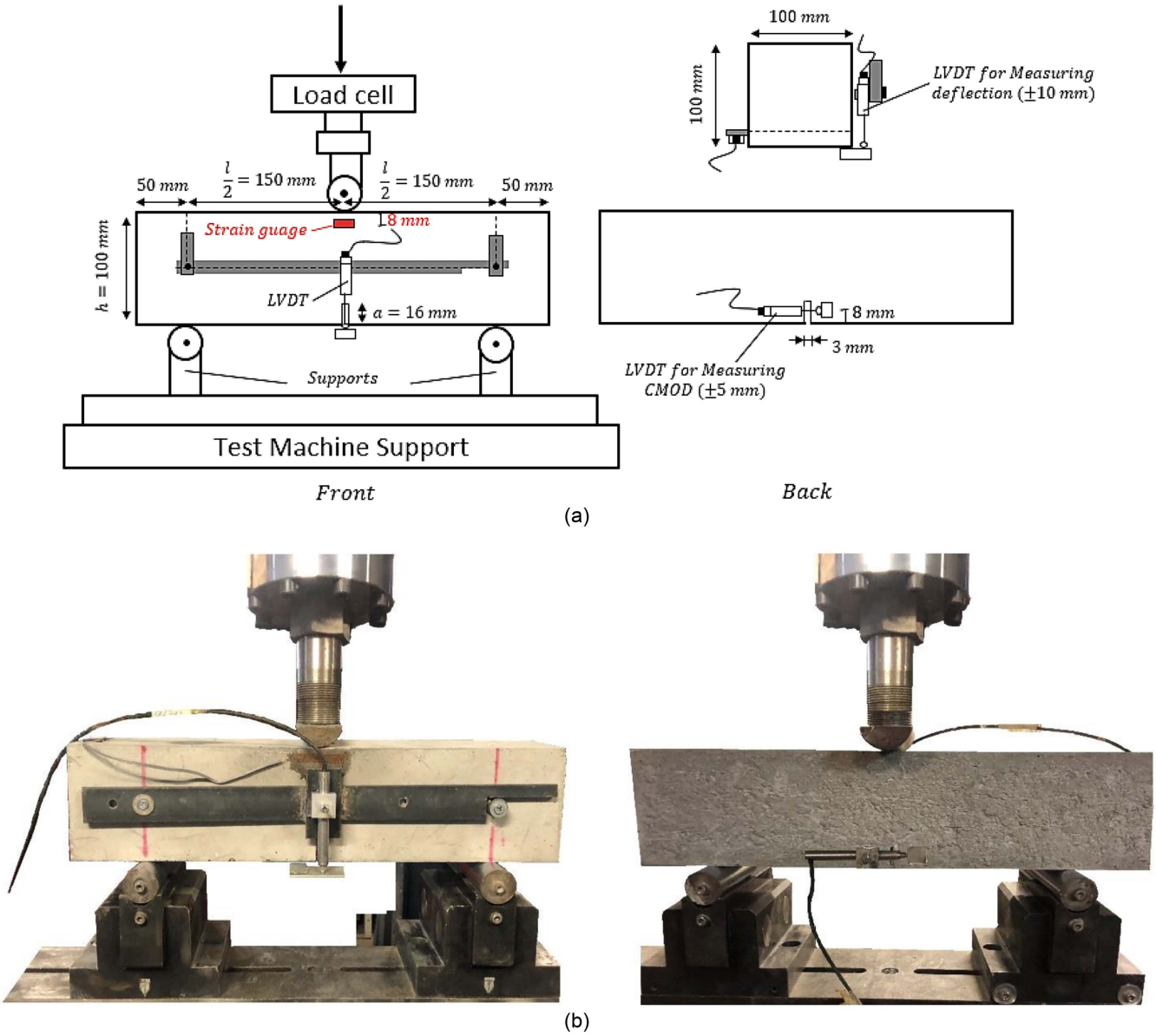

Fig. 1. Test configuration of 3PNBBT and the system used to monitor: (a) schematic view; and (b) images obtained during testing.

the beam to obtain the midspan deflection using the integral method. A total of 12 prismatic specimens were tested in four different impactor heights to assess the impact of the strain rate on the flexural tensile strength of SFRC. The load cell fixed to the hammer was used to measure the impact force between the hammer and the beam, and the contact velocity was determined by the drop height and gravitational acceleration. The hammer velocity evolution during the impact period was calculated by considering the contact velocity and the integral of the acceleration evolution recorded by the accelerometers. The evolution of loading point displacement was then determined by integrating the velocity of the hammer

$$\dot{\delta}(t) = \int \ddot{\delta}(t)dt \tag{3}$$

$$\delta(t) = \int \dot{\delta}(t)dt \tag{4}$$

The equation shows the relationship between the acceleration, $\ddot{\delta}(t)$, velocity, $\dot{\delta}(t)$, and deflection, $\delta(t)$, measured at the midspan of the beam. Additionally, following RILEM TC 162-TDF and EN 14651, the flexural strength of a notched beam under center-point loading is determined by the maximum reaction force, $P_{\max}$:

$$f_{ft} = \frac{3P_{\max}l}{2b(h-a)^2} \tag{5}$$

The average deflection history of the specimen during loading was directly captured by a high-speed camera and, indirectly, by two accelerometers. The high-speed camera was a PHOTRON APX-RS and was used to capture images with a resolution of 128 × 256 pixels during the impact process at a frequency of 15,000 Hz. The necessary illumination for capturing high-speed videos was provided by installing four halogen lamps. The collected images were subsequently used to obtain the displacement fields at the surface of the specimens, adopting the digital image correlation (DIC) technique. DIC is based on tracing speckles in deformed images and comparing them with speckles in the reference image within the selected area of interest (AOI). The deformations as well as

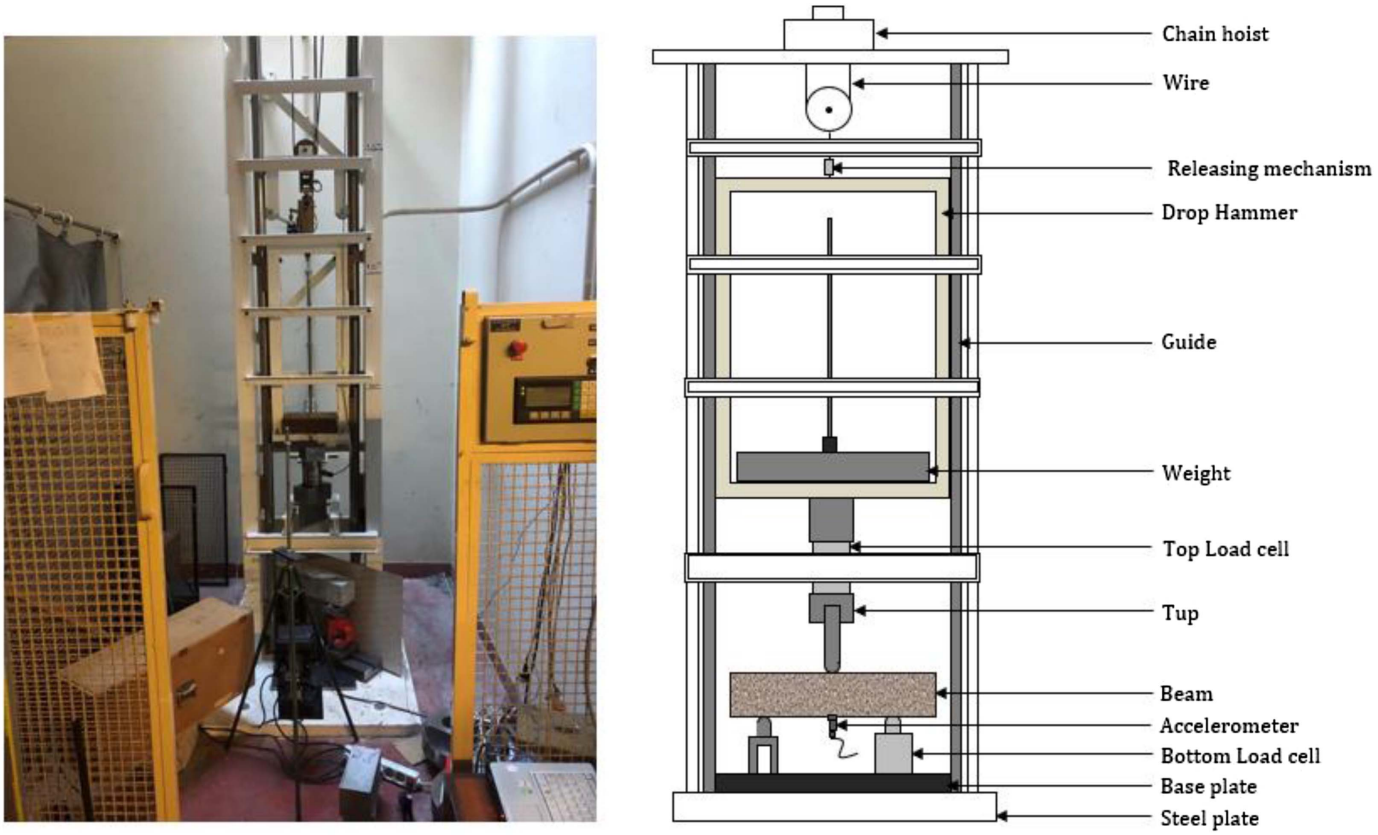

Fig. 2. Specimen under impact test and schematic representation of the drop weight impact machine.

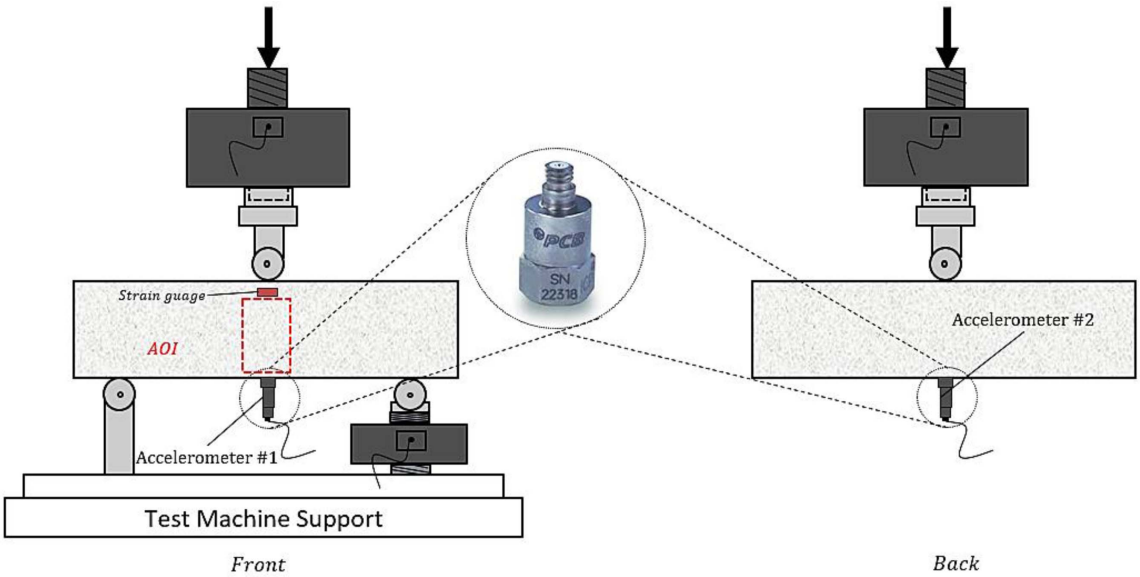

Fig. 3. Identification of the AOI for DIC and the positioning of all instrumentation.

the displacements may be computed based on the differences between original and deformed coordinates (Bhowmik and Ray 2019; Rasheed and Prakash 2018).

Fig. 3 shows the test setup and the AOI defined for imaging and subsequent image processing, as well as the positioning of the instrumentation and the test setup. The deflection of the beam specimens was obtained by averaging the vertical displacements obtained in all points of the AOI using DIC. In addition, the crack propagation, failure pattern, and fracture surfaces were investigated using DIC and GOM Correlate software.

The first image of each specimen was used as a reference for measuring the deformations and the crack lengths. The midspan

deflection and tensile and compressive strains obtained were compared to the analytical values of midspan deflection and strains obtained from Eqs. (2)–(4).

The strain rate was calculated using Eqs. (6) and (7), where the modulus of elasticity (E) was obtained from the compressive strength tests previously carried out at static strain rates, in line with the research of Othman et al. (2019)

$$\dot{\sigma} = \frac{\dot{M}y}{I} = \frac{3\dot{P}l}{2b(h-a)^2} \tag{6}$$

$$\dot{\sigma} = E\dot{\varepsilon}, \qquad \dot{\varepsilon} = \frac{3\dot{P}l}{2Eb(h-a)^2} \tag{7}$$

where I = moment of inertia of the beam's cross section; and $\dot{P}$ = maximum loading rate, obtained by identifying the peak slope in the reaction force time history.

An *equivalent static force* method was proposed to calculate the dynamic fracture energy (Zhang et al. 2014). In the quasi-static range of loading, although all beams failed in flexure at a wide range of loading rates, all specimens were not entirely broken. Therefore, the area under the load-midspan deflection diagram up to a specified deflection was used to evaluate the fracture energy (G_f). The following equation was used to obtain the value of fracture energy under both static and dynamic loading based on the experimental force–deflection curves of SFRC beams at various strain rates

$$G_f = \frac{W_0}{b(h-a)} + \frac{mg\delta_u[1-\frac{(l+2s)}{2l}]}{b(h-a)} \tag{8}$$

The RILEM TC50-FMC Technical Committee (RILEM 50-FMC Committee 1985) proposed the following equation for calculating the fracture energy under quasi-static loading conditions based on the experimental force–deflection curves of SFRC beams. The equation involves six parameters: W_0, b, s, m, δ_u, and g which correspond to the area under the load–displacement curve, the width of the specimen's cross section, the length of the cantilever parts of the beam, the mass of the specimen portion between supports (length l), the final deflection of the specimen, and the gravity acceleration, respectively. The equation consists of two parts. The first part calculates the fracture energy required for crack formation and propagation up to fracture, while the second part calculates the fracture energy absorbed by the specimen due to its self-weight (RILEM 50-FMC Committee 1985).

Table 4 summarizes the series of tests performed and the corresponding adopted displacement rates. The tests were named S, Q, and HS, signifying static, quasi-static, and high strain rate tests, respectively. In the present study, the minimum value of displacement rate in the range of quasi-static (0.3 mm/min) was considered as static loading. The number that follows Q in the quasi-static tests indicates the displacement rate (mm/min), but for high strain rate tests (impact tests), the number that follows HS indicates the height of the impactor (mm). For each specimen ID, three specimens were tested.

Table 4. Prismatic specimens at different loading rates

Specimen ID	Displacement rate (mm/min)	Height of impactor (mm)
S	0.3	—
Q18	18	—
Q120	120	—
Q500	500	—
HS250	—	250
HS500	—	500
HS1000	—	1,000
HS1500	—	1,500

Test Results and Discussion

Fracture Modes and Surface Analysis of Failed Specimens

Fig. 4(a) illustrates the failure modes of beams subjected to low loading rates in the quasi-static range. In these tests, one main crack and some branch cracks surrounding this main crack were identified at the midspan. When comparing the crack patterns of the different test series, fewer branch cracks were observed around the main crack in the case of the quasi-static tests, as opposed to the more pronounced crack branching observed in beams under impact loading.

The failure pattern of SFRC beams under different loading rates is largely determined by the interaction between the concrete and fiber interface. When tested under quasi-static loading conditions, the steel fibers were observed to be pulled out, whereas under impact load, both pull-out and tensile rupture of fibers were observed, as shown in Fig. 4. Increasing the drop weight height led to an increase in the number of ruptured fibers, but the dominant fracture mode remained the fibers being pulled out. The percentage of ruptured fibers increased with the drop height and was 2.3%, 4.1%, 6.9%, and 11.5% for dropping heights of 250, 500, 1,000, and 1,500 mm, respectively. This phenomenon is attributed to the shape of hooked-end steel fiber in SFRC. The hooked ends of the steel fibers provide anchorage, which increases resistance to pull-out. Since the rate sensitivity of the steel is lower than the matrix (Zanuy and Ulzurrún 2017), increasing the drop height causes a significant increase in the bond strength between the fiber and matrix. Under impact loading, the tensile stress in some steel fibers reached their ultimate strength leading to rupture. This phenomenon is intensified with the increase in drop height and the subsequent increase in the number of ruptured fibers.

Midspan Deflection and Strain Rate

Fig. 5 compares the midspan deflection in specimen HS1500-2 (as representative of the tested specimens) that was obtained by double integrating the acceleration history measured with the accelerometers using Eqs. (3) and (4), and also the one directly measured using the DIC technique. For all specimens, the midspan deflection obtained with DIC was higher than the deflection obtained with the pair of accelerometers. This can be attributed to the fact that DIC calculates the deflection directly (average of the points in the selected monitoring window), while double integrating the acceleration history considers time for calculating the deflection. Also, the accelerometers were placed at the midspan of the beam and bottom face of the specimens and the calculated acceleration was considered as the acceleration along the cross section of specimens. Comparing two used approaches to find the beam's midspan deflection has shown that both monitoring strategies can satisfactorily obtain the midspan deflection. In the use of accelerometers, it should be noted that at least two accelerometers should be used in the test, and the safety of the accelerometers should be considered during the impact test. The present research utilized results obtained from DIC analysis of experimental tests to determine the

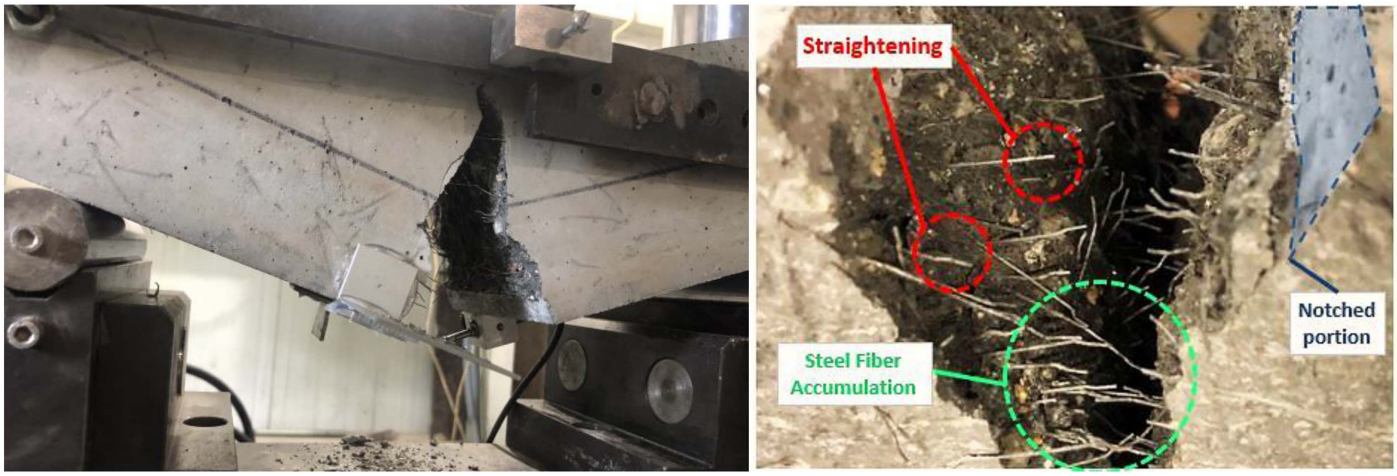

Fig. 4. Failure pattern of SFRC specimens: (a) quasi-static; and (b) impact loading.

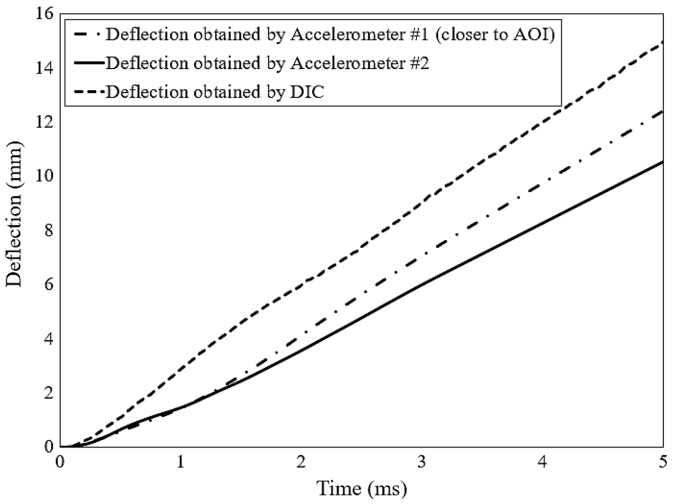

Fig. 5. Comparison of the deflection-time experimental responses obtained from DIC and the two accelerometers with one of the HS1500-2 specimens.

deflection of SFRC beams. However, it was found that the deflection results obtained by double integrating the beam's acceleration history showed a strong correlation with those obtained from the DIC method.

Two different approaches were used to determine the maximum strain rate in the tested specimens: (1) the strain history measured by the strain gauge installed in the compressive zone, assuming that the tensile and compressive strain rates are the same in uncracked and cracked SFRC; and (2) strain calculated from the maximum displacement rate using Eq. (2), assuming that the equation is also applicable to the post-cracked stage of the specimen. In the second approach, the maximum displacement was measured using an LVDT in the quasi-static tests and calculated by integrating the acceleration history using Eq. (3) in impact tests. Fig. 6 illustrates the typical midspan acceleration, midspan deflection, strain, and strain rate over time for specimen HS1500-2 subjected to an impact from a height of 1,500 mm. The acceleration histories obtained by the two accelerometers show approximately the same trend. However, since SFRC is not an isotropic material, some differences can be found in the response. Table 5 indicates the maximum strain rate recorded by the strain gauge and the average strain rate calculated with Eq. (2), whose results are graphically represented in

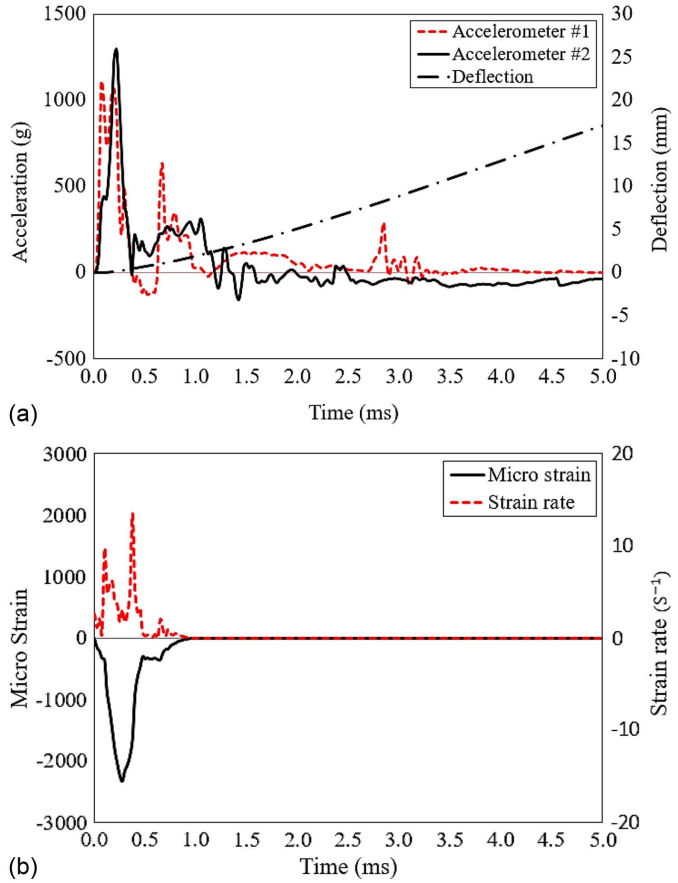

Fig. 6. Midspan acceleration, deflection, strain, and strain rate versus time for one of the HS1500 2 specimens: (a) acceleration and deflection; and (b) strain and strain rate.

Table 5. Recorded and calculated strain rate

Sample	Maximum strain rate (s^{-1}) SG[a] (directly)	Maximum strain rate (s^{-1}) Eq. (2) (indirectly)	Sample	Maximum strain rate (s^{-1}) SG[a] (directly)	Maximum strain rate (s^{-1}) Eq. (2) (indirectly)
S-1	3.41×10^{-6}	1.56×10^{-5}	HS250-1	2.23	4.46
S-2	3.41×10^{-6}	1.56×10^{-5}	HS250-2	4.49	4.68
S-3	3.41×10^{-6}	1.56×10^{-5}	HS250-3	5.87	4.51
Q18-1	1.00×10^{-4}	3.75×10^{-4}	HS500-1	4.43	5.92
Q18-2	1.00×10^{-4}	3.75×10^{-4}	HS500-2	11.09	6.13
Q18-3	1.00×10^{-4}	3.75×10^{-4}	HS500-3	6.64	6.55
Q120-1	5.52×10^{-3}	6.25×10^{-3}	HS1000-1	9.08	6.67
Q120-2	5.52×10^{-3}	6.25×10^{-3}	HS1000-2	10.12	9.96
Q120-3	5.52×10^{-3}	6.25×10^{-3}	HS1000-3	8.74	7.07
Q500-1	5.56×10^{-2}	2.60×10^{-2}	HS1500-1	9.71	6.22
Q500-2	5.56×10^{-2}	2.60×10^{-2}	HS1500-2	13.49	8.19
Q500-3	5.56×10^{-2}	2.60×10^{-2}	HS1500-3	13.37	9.10

[a]SG = strain gauge.

Fig. 7. As shown in Fig. 7, the differences between the obtained strain rates by the two methods in the quasi-static tests are more pronounced than in the impact tests. These differences are related to the fact that, in Eq. (2), it is assumed the SFRC shows linear-elastic behavior. The results obtained from the direct and indirect measurements were similar up to crack initiation, but beyond this stage, the strain rates differed when assuming linear-elastic behavior. The utilization of indirect measurement to determine strain and strain rate values is limited to crack initiation. Furthermore, inaccuracies in results can arise when assuming linear-elastic behavior, particularly when subjected to impact loads. As a result, the indirect measurement is not recommended to obtain strain and strain rate during the impact process. To address these concerns, the present study directly utilized measured strain values, obtained by strain gauges, as the best monitoring strategy to investigate the rate sensitivity of SFRC.

Impact, Reaction and Inertia Forces

In the tests performed, the reaction force was calculated by doubling the load measured by the bottom load cell, considering the symmetry of the test setup (Ulzurrun and Zanuy 2017; Yoo et al. 2015). The first peak identified in the time history of the impact force corresponds to the load capacity provided by the dynamic tensile strength due to the fact that the first peak load increases with the height of the impactor. The post-peak response of the specimens subjected to the larger height of the impactor shows some smaller load peaks, as shown in Fig. 8. For deflections above the one corresponding to the post-peak, the behavior of SFRC under impact loading is mainly controlled by fiber bridging. If the peak loads are reduced during the post-peak stage, the fiber-resisting mechanisms will be less significant in magnitude (Park et al. 2017).

A delay in time was noticed between the reaction force responses and the impact force due to the time taken by the shear stress wave to travel from the midpoint of the beam, where it was impacted, to the supports. The time delay experimentally measured for SFRC specimens under impact loadings has decreased with increasing impact velocity (or height of impactor), having been registered time delays of 620, 551, 275, and 170 μs for impactor heights of 250, 500, 1,000, and 1,500 mm, respectively. Figs. 9 and 10 illustrate the reaction force-midspan deflection diagrams at different quasi-static displacement rates and for different heights of the impactor, respectively.

The loading time needed to attain the maximum reaction force for the impactor dropping heights of 250, 500, 1,000, and 1,500 mm is shown in Fig. 11, which shows decreases with increases in dropping height of the impactor. Consequently, both contact velocity and the strain rate in the specimens increase for increased dropping height of impactor.

The inertial force (P_i) directly affects the mechanical response of the specimen under impact loading and, therefore, appropriate dynamic analysis is necessary. For this purpose, the reaction force (P_b) must be used to analyze the flexural behavior of the beam. The reaction force was considered as the bending force, which can be a fraction of the impact load. As shown in Fig. 12, the impact is approximately a point load at the specimen midspan, while the inertial force is a distributed load along the specimen that acts in the opposite direction of the beam deflection, and two symmetric reaction loads are assumed in the supports. By generalizing the distributed inertial force to a point load and using the dynamic equilibrium equation, the reaction force is the difference between the impact force and the inertial force, as shown in Eq. (9). For a virtual deflection (δ_v) of the beam that is compatible with its support conditions, the virtual work expression can be written for calculating the value of the inertial force (Banthia et al. 1989), according to Eq. (10)

$$P_t = P_b + P_i \tag{9}$$

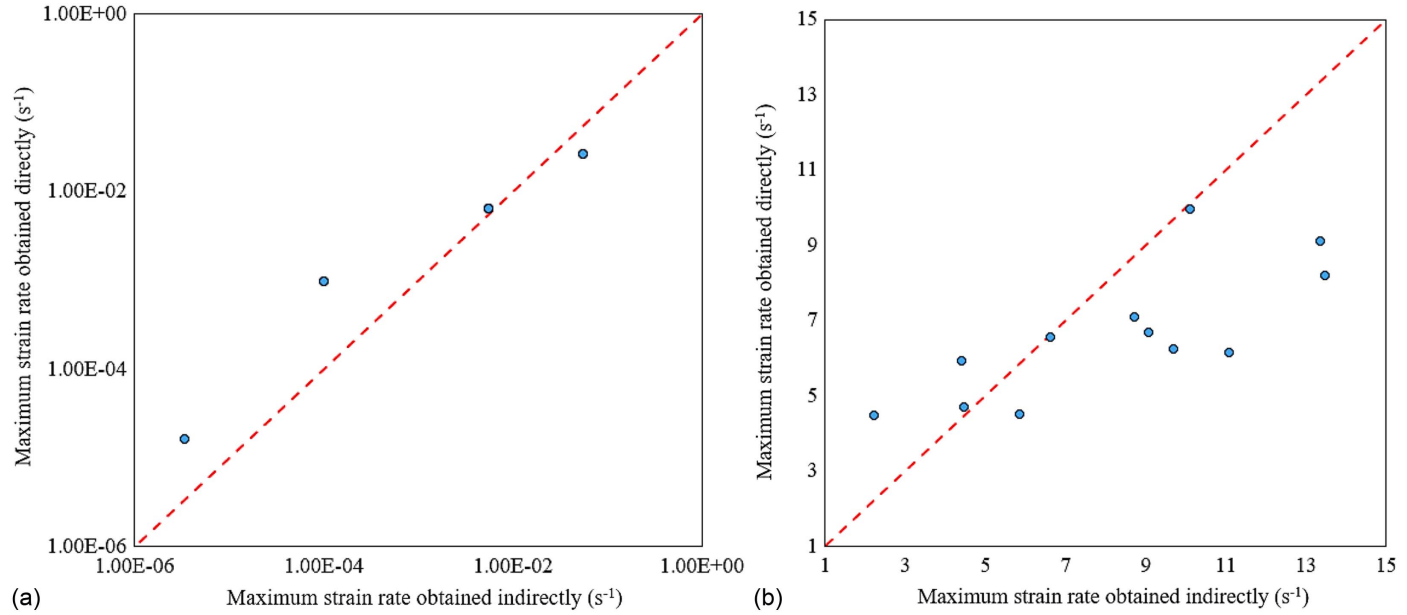

Fig. 7. Maximum strain rates calculated by Eq. (2) (indirectly) and measured from strain gauge (directly): (a) quasi-static; and (b) drop weight impact.

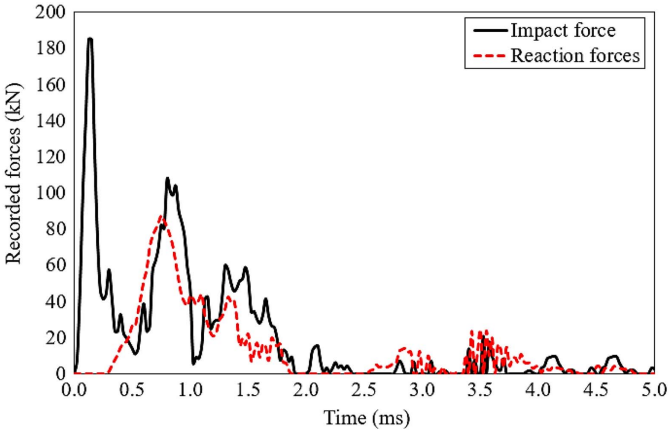

Fig. 8. Typical history of impact and reaction forces over time for one of the HS1500-2 specimens.

$$P_i(t)\Delta\delta_v(x,t) = \int_0^l \rho A\ddot{\delta}(x,t)\Delta\delta(x,t)dx + 2\int_l^{l+s} \rho A\ddot{\delta}(x,t)\Delta\delta(x,t)dx \quad (10)$$

where $\ddot{\delta}(x,t)$ is the acceleration at a specific section along the beam; $\Delta\delta(x,t)$ is the virtual deflection at a specific section along the beam; ρ is the density of the materials used in the beam; and A, l and s are the cross-sectional area, span length, and overhanging length, respectively.

To simplify the calculation of the inertial force, two distributions, either linear or sinusoidal, can be used to express acceleration and inertial force along the beam. In the present study, a linear distribution is used to define the acceleration along the beam. Consequently, Eq. (11) shows the appropriate simplified equation to include only the values of midspan acceleration (Banthia et al. 1989, 1987)

$$P_i = \rho A\ddot{\delta}_{\max}\left[\frac{l}{3} + \frac{8}{3}\frac{s^3}{l^2}\right] \quad (11)$$

By calculating the inertial force (P_i), the bending force (P_b) of the beam is obtained and the real dynamic beam may be replaced by an equivalent static beam, as proposed in Fig. 12. Using the dynamic equilibrium, as well as the assumption that acceleration and inertial force have a linear variation along the beam, the reaction force in each support is obtained

$$P_b = P_t - \rho A\ddot{\delta}_{\max}\left[\frac{l}{3} + \frac{8}{3}\frac{s^3}{l^2}\right] \quad (12)$$

Results from tests carried out with SFRC beams in the current study support the assumption made by Bentur et al. (2006) that the accelerations and displacements along the length are linearly distributed. In the present study, the reaction force was obtained by doubling the amount of force measured in one of the supports, assuming symmetry in the system (Banthia et al. 1987), Table 6.

Fig. 13(a) shows the comparison of experimentally and analytically calculated inertial forces. The absolute fraction of variance (R^2) and the mean absolute percentage error (MAPE) between the experimental and analytically calculated inertial forces correspond to, respectively, 0.83 and 26%. As shown in Fig. 13(a), the analytical equation can acceptably predict the inertial force. In addition, the average of the inertia to impact load ratio is 0.6, which seems to be independent of the strain rate, as shown in Fig. 13(b), where the results reported by Ulzurun and Zanuy (2017) and Banthia et al. (1987) are also included and support this observation. Although there are not many experimental results about the strain rate effect on the inertial force in SFRC beams, it seems that the strain rate effect on the inertia to impact load ratio is not significant. These conclusions are limited to the testing conditions and assumptions adopted in the present study.

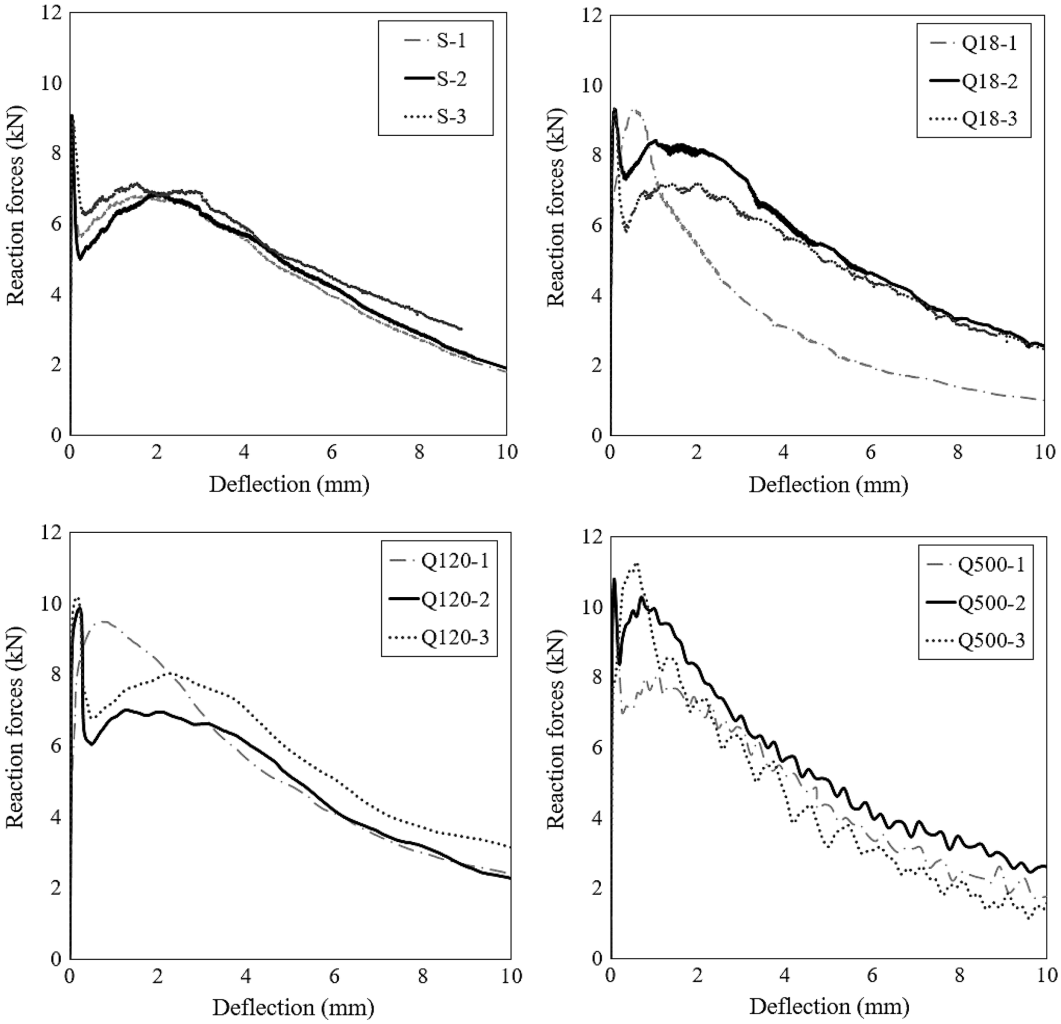

Fig. 9. Reaction force-midspan deflection diagrams for the specimens tested in static and quasi-static loading.

Effect of Strain Rate on Flexural Behavior of SFRC

Flexural Tensile Strength, $\mathbf{DIF}_{ft}$

In the present research, since the impact force measured by the top load cell includes the inertial force, the maximum reaction force was considered in the calculation of the SFRC flexural tensile strength. The obtained mechanical characteristics of the specimens tested at the static tensile strain rate of 3.41×10^{-6} s^{-1} are shown in Table 7. The energy dissipated during the fracture process up to the maximum recorded deflection, herein abbreviated by fracture energy, was calculated from Eq. (8). Since the SFRC beams were not completely broken during the test, the area under the reaction force–deflection diagram at the beams' midspan up to a specified deflection was used to evaluate the fracture energy. This method was adopted in previous studies (Akcay and Tasdemir 2012; Banthia et al. 1998; Gopalaratnam and Shah 1986; Naaman and Gopalaratnam 1983; Suaris and Shah 1983; Zhang et al. 2014). In the present study, a cutoff point was selected, a midspan deflection of 2 mm, for all tests under both quasi-static and impact loading, discussed in detail in Section 3.4.2.

A total of 21 specimens were tested to investigate the strain rate effect on flexural tensile strength and fracture energy. Experimental results of three-point bending tests under quasi-static and impact loading are shown in Table 8. For calculating DIF, the average flexural tensile strength and fracture energy of the static strain rate (series S) are considered as references. The obtained results show that the flexural tensile strength and the fracture energy of SFRC specimens exhibit sensitivity to the applied strain rate. The DIF values for flexural tensile strength ($DIF_{f_{ct,fl}}$) and fracture energy (DIF_G) were determined for each specimen and then compared with previously established DIF models. This was done to evaluate whether these models are capable of accurately predicting the impact of strain rate on these characteristics of the SFRC that was developed.

The flexural tensile strength ($f_{ct,fl}$) has shown an increase with the strain rate, as well as the gradient of $f_{ct,fl}/\dot{\varepsilon}$. The coefficient of variation obtained for the flexural tensile strengths at different strain rates (quasi-static or impact range) varied between 0.2% and 13.5%.

The models proposed by CEB-FIP (CEB-FIP 1990, 2010) were used to evaluate the DIF of the tensile strength (direct tensile or splitting tensile) obtained at the strain rate ranges of quasi-static and impact. The DIF of tensile strength was also evaluated considering the models proposed by Malvar and Ross (1998), Tedesco and Ross (1998), Fujikake et al. (2006), and Tran and Kim (2013), which are described in Appendix. Malvar and Ross (1998) proposed a model for DIF of splitting tensile strength ($DIF_{f_{ct,SHPB}}$) based on experimental results obtained for plain concrete and split Hopkinson pressure bar (SHPB) testing, instead of the three-point bending test. They reported that the available data

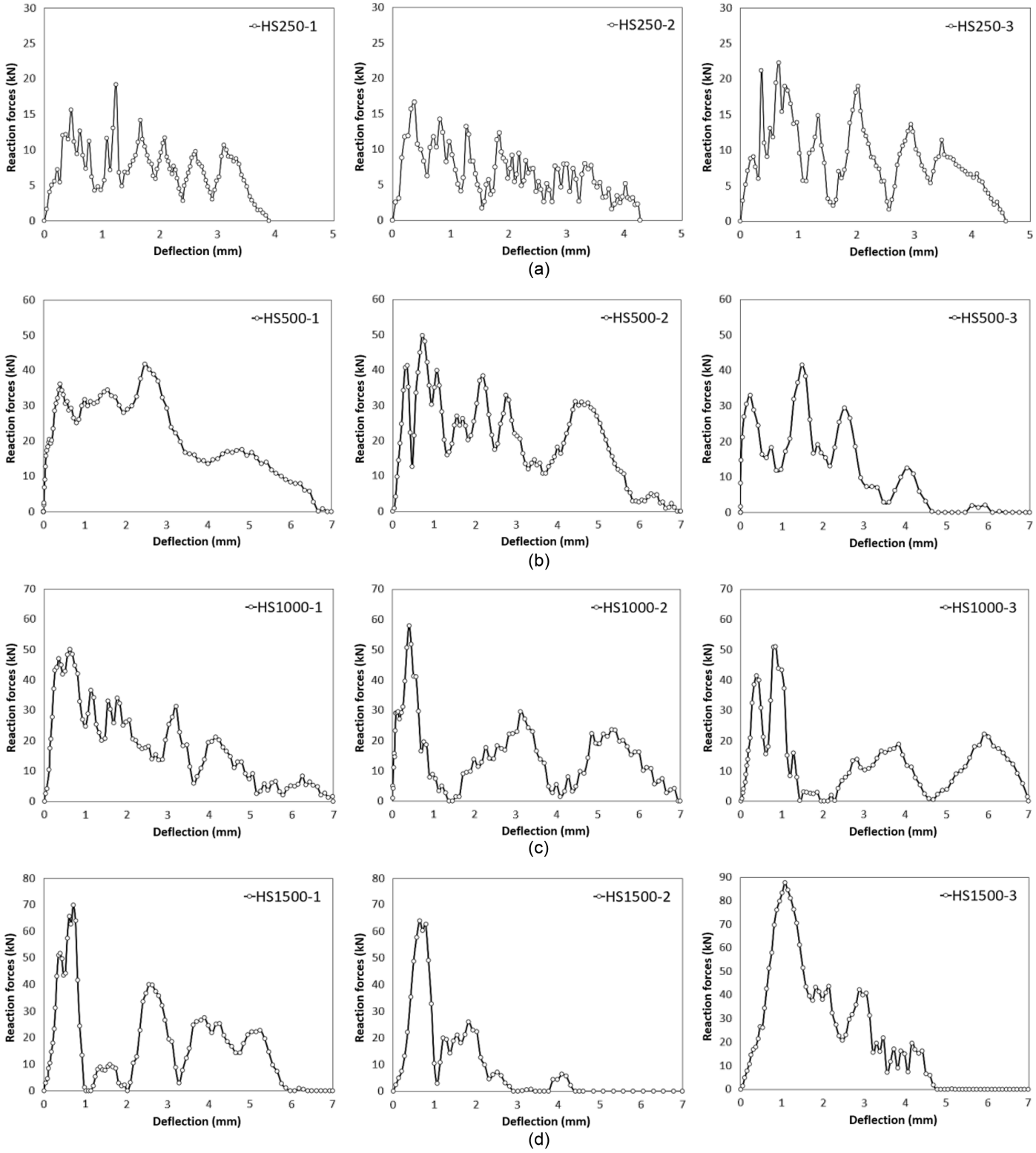

Fig. 10. Reaction force-midspan deflection diagrams for the specimens subjected to different heights of the impactor: (a) 250 mm; (b) 500 mm; (c) 1,000 mm; and (d) 1,500 mm.

at high strain rates seems to support that the change in slope occurs close to 1 s^{-1} instead of at 30 s^{-1} as assumed by CEB-FIP (CEB-FIP 1990). Tedesco and Ross (1998) proposed a model for the dynamic tensile strength of concrete materials under high strain rates and they used the results obtained from SHPB tests for calibrating the model's parameters. Fujikake et al. (2006) suggested an alternative model using experimental results from reactive powder concrete reinforced with short steel fibers. Since the models by previous studies (CEB-FIP 1990, 2010; Fujikake et al. 2006; Malvar and Ross 1998; Tedesco and Ross 1998; Tran and Kim 2013) were proposed based on the experimental results using different test setups, they were compared in the present

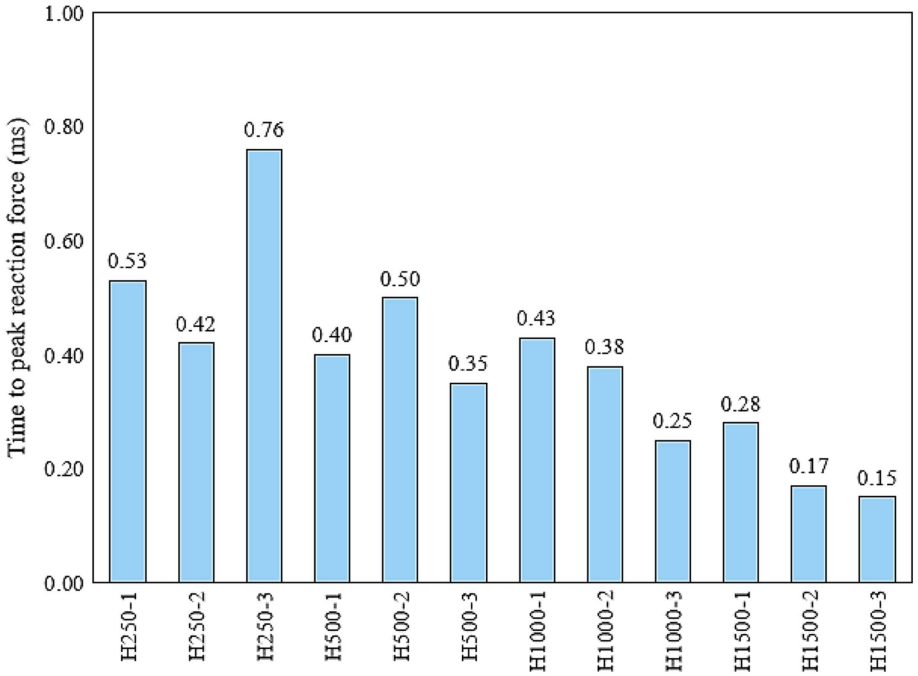

Fig. 11. Time at peak reaction force for different heights of impactor.

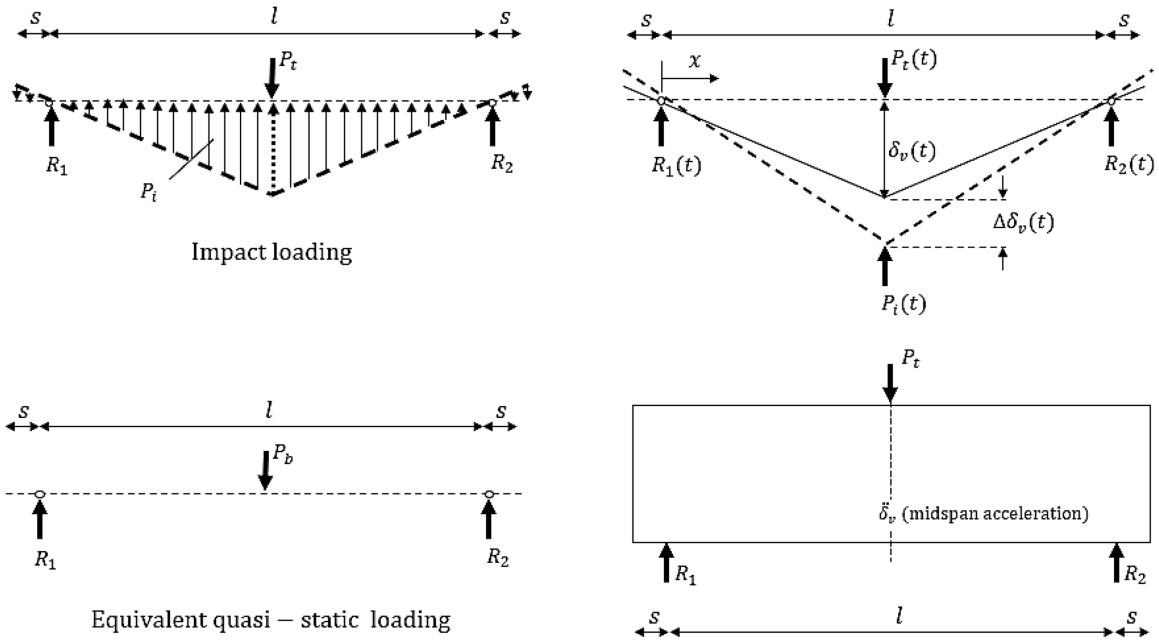

Fig. 12. Generalization of inertial force.

study to show the effect of the test setup on the prediction of the DIF of tensile strength. For this purpose, three different DIFs have been used, $\mathrm{DIF}_{f_{ct,\mathrm{direct}}}$, $\mathrm{DIF}_{f_{ct,\mathrm{SHPB}}}$, and $\mathrm{DIF}_{f_{ct,fl}}$ corresponding to tensile strength DIF obtained from the direct tensile, SHPB, and three-point bending tests, respectively, and their formulations are presented in the Appendix.

Fig. 14 compares the experimental results obtained in the present research with those found in the literature (Gao et al. 2020; Millard et al. 2010; Othman et al. 2019; Suaris and Shah 1982; Ulzurrun and Zanuy 2017; Yoo et al. 2015, 2016; Yoo and Banthia 2017; Zanuy and Ulzurrún 2017; Zhang et al. 2014). In general, the results obtained are in agreement with the ones obtained by other authors, where a smooth increase of flexural tensile strength, up to a strain rate of about 1 s^{-1}, is followed by a steeper increase, corresponding to the results obtained using the drop weight impact test. Various researchers and codes have suggested that a strain rate of 1 s^{-1} serves as a transitional point in DIF models for tensile strength. Nevertheless, more experimental results are required for assessing the effect of shape and volume fraction of steel fibers on the $\mathrm{DIF}_{f_{ct,fl}}$ of SFRC.

The proposed models must consider the type of loading (test approach) and the strain rate in predicting the values of both the

Table 6. Summary of obtained impact, reaction, and inertial forces corresponding to the maximum load capacity of the beam

Sample	Strain rate (s^{-1})	Impact force, P_t (kN)	Reaction forces, P_b[a] (kN)	Inertia force, P_i (kN)		P_i/P_t	
				$P_t - P_b$ (directly)	Eq. (12) (indirectly)	Directly	Indirectly
HS250-1	2.23	67.69	31.25	36.44	57.08	0.54	0.84
HS250-2	4.49	63.69	33.24	30.44	36.85	0.48	0.58
HS250-3	5.87	76.56	44.52	32.04	45.08	0.42	0.59
HS500-1	4.43	106.14	41.53	64.62	75.45	0.61	0.71
HS500-2	11.09	114.85	41.76	73.10	66.12	0.64	0.58
HS500-3	6.64	89.21	49.84	39.37	60.95	0.44	0.68
HS1000-1	9.08	148.22	58.04	90.18	57.25	0.61	0.39
HS1000-2	10.12	147.32	51.01	96.31	84.29	0.65	0.57
HS1000-3	8.74	138.08	48.47	89.62	102.19	0.65	0.52
HS1500-1	9.71	173.81	63.96	109.85	147.26	0.63	0.85
HS1500-2	13.49	185.16	87.45	97.72	98.21	0.53	0.45
HS1500-3	13.37	183.58	69.81	113.77	116.48	0.62	0.51

[a]Reaction force was obtained by doubling the amount of force measured by one of the supports, assuming symmetry in the system (Banthia et al. 1987).

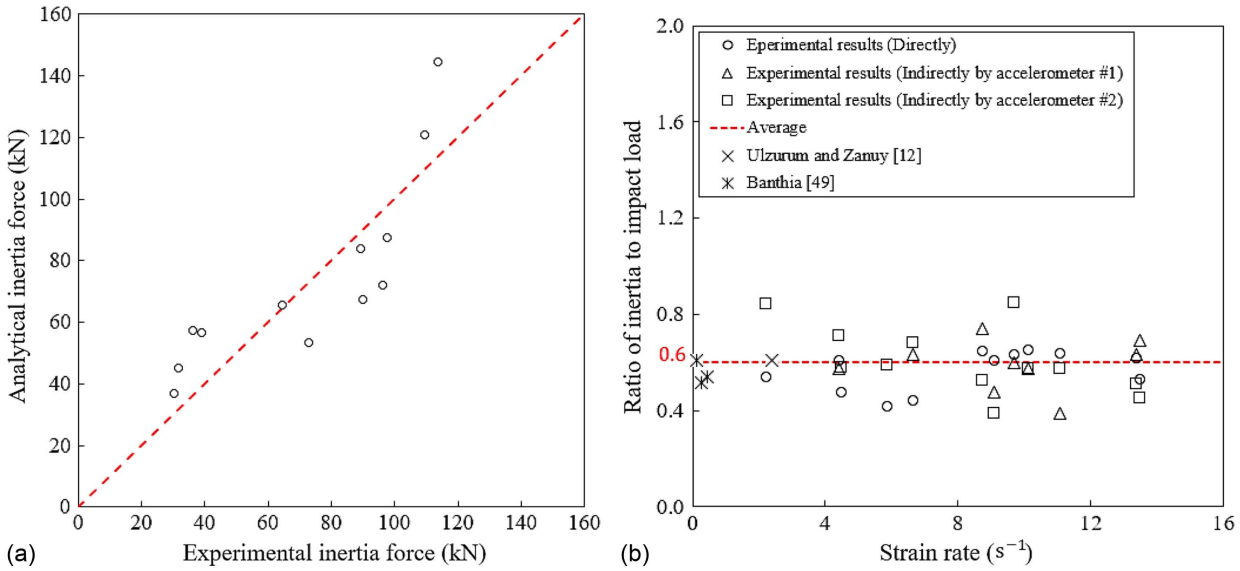

Fig. 13. (a) Comparison of analytical and experimental results of inertial force; and (b) inertia to impact force ratio versus strain rate.

flexural tensile strength and fracture energy. For this purpose, an empirical relationship was proposed for each range of loading, one in the quasi-static range and another in the range of impact, and the corresponding mechanical characteristic, to explain the strain rate sensitivity of SFRC in drop weight impact tests

$$\mathrm{DIF}_{f_{ct,fl}}^{\text{Quasi-static}} = \left(\frac{\dot{\varepsilon}_c}{\dot{\varepsilon}_{cs}}\right)^{A\times 10^{-3}}, \qquad \dot{\varepsilon}_c \le \dot{\varepsilon}_{tr} \tag{13}$$

Table 7. Specimens tested at static strain rate (3.41×10^{-6} s^{-1})

Type ID	Flexural tensile strength (MPa)	Fracture energy ($N \cdot m^{-1}$)
S-1	5.72	5,590
S-1	5.79	5,575
S-3	5.73	6,055
Average	5.75 (0.5)	5,740 (4.1)

Note: Values in parentheses are the coefficient of variation (in percentage).

$$\mathrm{DIF}_{f_{ct,fl}}^{\text{Drop weight}} = B \times 10^{-7}\left(\frac{\dot{\varepsilon}_c}{\dot{\varepsilon}_{cs}}\right) + C, \qquad \dot{\varepsilon}_c > \dot{\varepsilon}_{tr} \tag{14}$$

where $\mathrm{DIF}_{f_{ct,fl}}^{\text{Quasi-static}}$ and $\mathrm{DIF}_{f_{ct,fl}}^{\text{Drop weight}}$ are the dynamic increase factors for the quasi-static and drop weight impact ranges, respectively. The value of 1 s^{-1} was proposed for the transition strain rate ($\dot{\varepsilon}_{tr}$) between the quasi-static and impact ranges associated with the drop weight test. Table 9 shows the coefficients proposed for the DIF on fracture energy of SFRC.

Fig. 14 shows and compares the $\mathrm{DIF}_{f_{ct,fl}}$ obtained considering both the experimental results, the models proposed by CEB-FIP (CEB-FIP 1990, 2010), the results obtained by other researchers, and the model proposed in the present work. As demonstrated in Fig. 14(a), the CEB-FIP models appear to slightly overestimate the flexural tensile strength in quasi-static tests but underestimate it in the impact range of strain rate, as indicated in Fig. 14(b). However, further experimental data is required to draw a conclusive finding. Moreover, several studies have reported that the DIF values for tensile strength obtained from flexural tests are greater than those

Table 8. Experimental results of three-point bending tests

Sample	Strain rate (s^{-1})	Peak flexural load[a] (kN)	Flexural tensile strength[b] (MPa)	$DIF_{f_{ct,fl}}$	Fracture energy ($N \cdot m^{-1}$)	DIF_G
S (Average)	3.41×10^{-6}	9.02	5.75 (0.5)	1.00	5,740 (4.1)	1.000
Q18-1	1.00×10^{-4}	9.31	5.94	1.033	4,002	0.696
Q18-2	1.00×10^{-4}	9.31	5.94	1.033	6,263	1.089
Q18-3	1.00×10^{-4}	9.35	5.96	1.037	6,067	1.055
Q120-1	5.52×10^{-3}	9.49	6.05	1.052	6,625	1.152
Q120-2	5.52×10^{-3}	9.88	6.30	1.096	6,327	1.100
Q120-3	5.52×10^{-3}	10.18	6.49	1.129	6,826	1.187
Q500-1	5.56×10^{-2}	10.49	6.69	1.163	6,951	1.209
Q500-2	5.56×10^{-2}	10.77	6.87	1.195	7,107	1.236
Q500-3	5.56×10^{-2}	11.27	7.19	1.250	6,023	1.047
HS250-1	2.23	31.25	14.06	2.445	8,158	1.421
HS250-2	4.49	33.25	14.96	2.602	6,746	1.175
HS250-3	5.87	44.53	20.04	3.485	7,669	1.336
HS500-1	4.43	51.27	23.07	4.012	6,296	1.095
HS500-2	11.09	41.76	18.79	3.268	9,663	1.680
HS500-3	6.64	49.84	22.43	3.901	7,995	1.390
HS1000-1	9.08	58.04	26.12	4.543	10,535	1.832
HS1000-2	10.12	51.02	22.96	3.993	11,871	2.064
HS1000-3	8.74	48.47	21.81	3.793	9,204	1.601
HS1500-1	9.71	63.96	28.78	5.005	12,530	2.179
HS1500-2	13.49	87.44	39.35	6.843	18,653	3.244
HS1500-3	13.37	69.82	31.42	5.464	14,042	2.442

[a]The maximum reaction force was assumed as the peak flexural load.
[b]Obtained by Eq. (5).

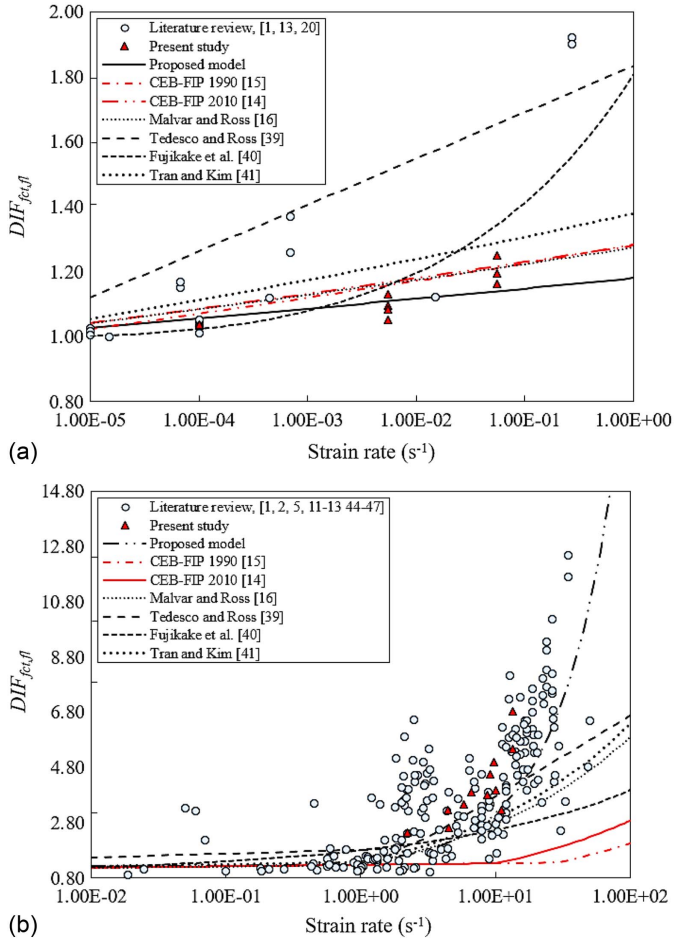

Fig. 14. Empirical DIF estimations of SFRC's flexural tensile strength for different test methods: (a) quasi-static; and (b) drop weight impact.

Table 9. Coefficients in proposed DIF formula for SFRC, according to Eqs. (13) and (14)

Parameter	A	B	C
$DIF_{f_{ct,fl}}$	27	1.92	1.23
DIF_G	34	0.58	1.53

Table 10. MAPE and MAD values for prediction of $DIF_{f_{ct,fl}}$ by different models

	Quasi-static			Drop weight impact		
Reference	R^2	MAD	MAPE	R^2	MAD	MAPE
Proposed model	0.701	0.08	6.5	0.712	1.16	29.0
CEB-FIP (1990, 2010)	0.487	0.09	6.8	0.381	2.45	52.4
CEB-FIP (1990, 2010)	0.486	0.10	7.4	0.509	2.36	50.8
Malvar and Ross (1998)	0.485	0.10	7.3	0.576	1.55	34.0
Tedesco and Ross (1998)	0.472	0.24	21.1	0.543	1.24	34.3
Fujikake et al. (2006)	0.490	0.09	6.6	0.576	1.71	39.9
Tran and Kim (2013)	0.674	0.12	9.1	0.557	1.43	32.6

acquired from direct tension tests (Gopalaratnam and Shah 1986; Naaman and Gopalaratnam 1983; Ulzurrun and Zanuy 2017; Zhang et al. 2009, 2014).

In order to evaluate the agreement between the different models, the R^2, mean absolute deviation (MAD), and (MAPE) were calculated for each parameter and each testing approach, as shown in Table 10. The results show that the model proposed by Tedesco and Ross (Tedesco and Ross 1998), with R^2, MAD, and MAPE values of 0.472, 0.24, and 21.1%, respectively, diverge most in the quasi-static range. The estimation of the $DIF_{f_{ct,fl}}$ was improved by the model proposed in the present study, with the lowest R^2, MAD, and MAPE values (Table 10). Most of the models analyzed in this

study were derived from experimental results obtained with the SHPB-split tensile test. Since the possible range of strain rate obtained with SHPB is generally higher than the one achievable by drop weight impact tests, these models seem to underperform when predicting the experimental $DIF_{f_{ct,fl}}$ obtained in three-point bending tests. This means that the type of test (SHPB, drop weight, direct tensile test, etc.) influences the measured strain rate sensitivity of SFRC. As shown in Fig. 14, the models proposed in the literature do not follow the trend of experimental results, especially when results obtained in the drop weight impact test are considered. The model proposed in the present study predicts the $DIF_{f_{ct,fl}}$ more accurately by considering the effect of both strain rate and type of test considered (quasi-static test and drop weight impact test). Therefore, an appropriate model should be selected to design the structural elements subjected to dynamic loading, according to the type of loading expected in the design of the structure.

Fracture Energy, DIF_G

Fig. 15 shows the load-crack mouth opening displacement (CMOD) measured in all SFRC specimens that were tested at four different strain rates in the range of quasi-static conditions by considering the average of the load registered in the three specimens of each series for each strain rate. Both the ascending (pre-peak) and descending (post-peak) portions of the load-CMOD curves depend on the strain rate. Generally, by increasing the loading rate, the flexural force increases, and the loss of load capacity immediately after peak load decreases.

It is attributed to the fact that both matrix and steel fibers in SFRC are sensitive to the loading rate. In fact, the fiber pull-out resistance and energy consumption increase with the loading rate, as well as the stiffness and strength of the surrounding matrix (Mujalli et al. 2022; Poveda et al. 2020; Tarifa et al. 2020), as long as tensile rupture of the fibers is avoided. This leads to a better crack opening arrestment by the fibers bridging a crack when the SFRC is subjected to higher loading rate conditions (Mujalli et al. 2022). This enhanced bridging and crack arrest mechanisms increase the stiffness of a SFRC member in its elasto-cracked stage and its load carrying capacity, not only up to peak load, but also in the structural softening stage. For instance, at a crack opening of 0.2 mm, which occurs already at the post-peak stage, the average values of the forces for loading rates of 0.3, 18, 120, and 500 mm · min^{-1} are 5.9, 7.7, 8.2, and 9.3 kN, respectively. Therefore, the fracture energy increases with increasing strain rates, agreeing with the DIF of fracture energy (DIF_G) presented in Table 8.

As mentioned previously, for three-point bending tests under both quasi-static and impact loadings, the chosen cutoff value in deflection was set at 2 mm for calculating the fracture energy using Eq. (8). Some of the specimens failed when the deflection reached approximately 2 mm (Fig. 16); therefore, this cutoff deflection establishes a term of comparison for all specimens. The analysis of results showed that the definition of a cutoff exceeding 2 mm would not result in a significant variation of the ratio between the obtained fracture energy and the reference fracture energy (using a complete curve without cutoff), for different strain rates. Similar results were reported by Zhang et al. (2014) for hooked-end SFRC beams. The coefficient of variation of fracture energy obtained at each strain rate (quasi-static range) or height of impactor (impact range) ranged between 4.1% and 18.7%, as presented in Table 8.

The strengthening efficiency of hooked-end steel fibers relies on the mechanical bond established with concrete and the two anchorages at either end. The contribution of each to dissipate energy can vary, depending on the strain rate considered (Banthia and Trottier 1991). Zhang et al. (2014) reported that due to the strong limitation in the displacement of anchored hooked-end fibers in the concrete and the local damage that occurs vicinity of the hooks, the hooked-end fiber has a relatively weaker bond performance than other steel fibers under impact loading. This limitation in the displacement of the fiber leads to a decrease in the ultimate strain of SFRC and thus a lower fracture energy, when compared to other types of steel fibers used in SFRC under impact. Consequently, the fracture energy under impact loading of SFRC with hooked-end fibers mainly depends on the anchorage contribution of the fibers (Banthia and Trottier 1991). Moreover, some experimental studies (Poveda et al. 2020; Tarifa et al. 2020) have investigated the effect of displacement pull-out rate of the steel fiber pull-out test. These have shown that the sensitivity of the experimental response of concrete with hooked-end fibers to strain rate is lower than the one measured in smooth fibers SFRC.

The literature shows that the bond behavior and mechanical characteristics and the mechanical properties of hooked-end steel fibers are the most relevant parameters influencing SFRC post-cracking behavior and fracture energy, especially under impact loading. Moreover, the pull-out load and mechanical properties

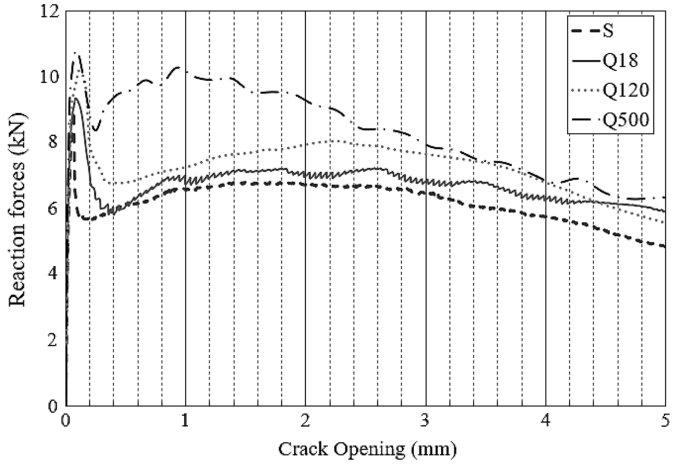

Fig. 15. Reaction forces-CMOD curves under quasi-static loading.

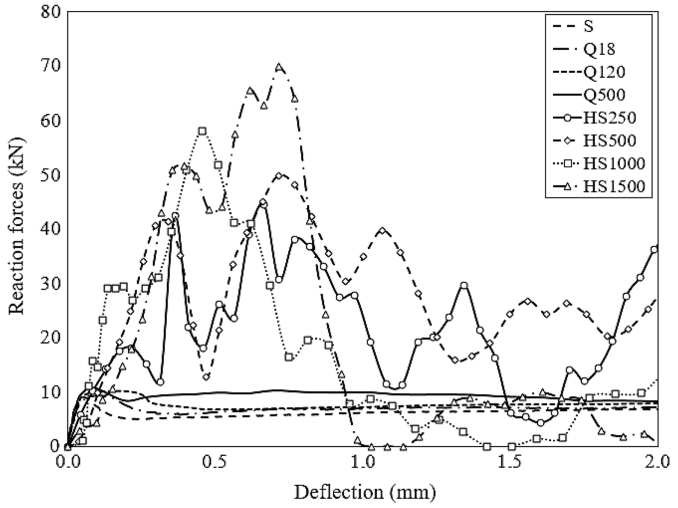

Fig. 16. Total reaction forces–deflection curves up to 2 mm of midspan deflection.

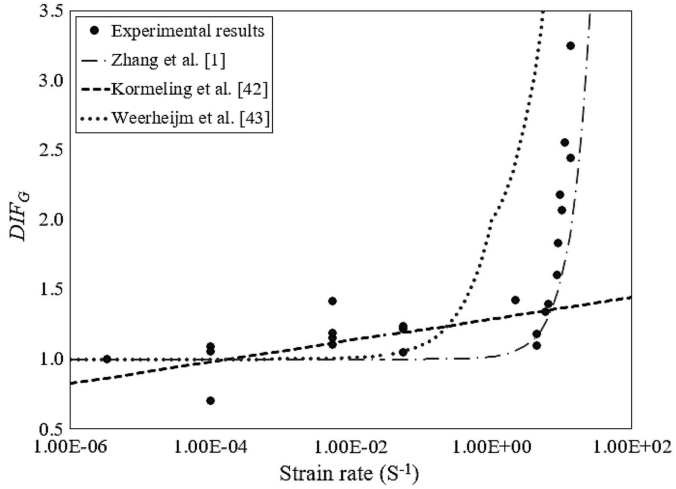

Fig. 17. Strain rate sensitivity of the fracture energy.

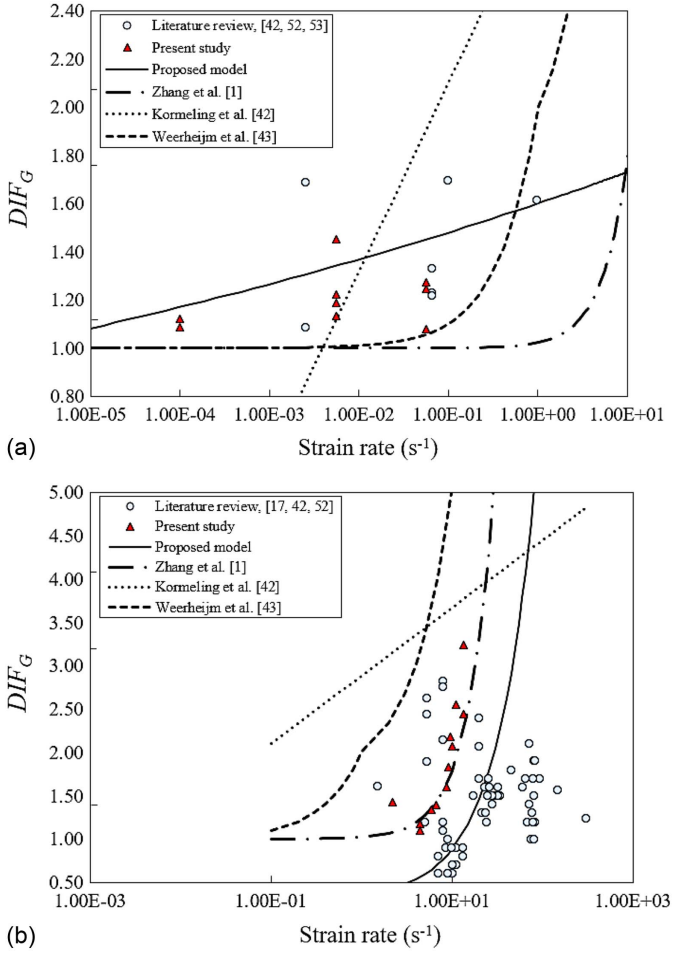

Fig. 18. Empirical DIF relations for SFRC's fracture energy using different test methods: (a) quasi-static; and (b) drop weight impact.

of hooked-end fibers play a crucial role in determining the fracture energy of SFRC specimens exposed to various loading rates. Table 8 presents the ratio of dynamic to static fracture energy for all tested SFRC specimens, which reveals that strain rate can significantly affect SFRC fracture energy. The maximum DIF for fracture energy shown in Table 8 is 3.24.

The effect of strain rate on the fracture behavior of SFRC is mostly related to the behavior of the matrix and the pull-out of fibers, because only a scarce quantity of broken fibers was found in the crack surface. As mentioned before, although the pull-out mechanisms are dominant under quasi-static loading, the straightening phenomenon is more visible when the strain rate is increased. This means that, for higher strain rates, the steel fibers carry more axial force while being pulled out from the matrix, which causes an increase in the flexural tensile strength of SFRC and an improvement of its post-peak behavior. Therefore, the rate sensitivity of steel fibers is the main reason for the loading rate sensitivity of SFRC. The effect of the loading rate on the fracture energy is also shown in Fig. 17. In the range of impact, the DIF model for fracture energy proposed by Zhang et al. (2014) can predict the obtained experimental results better than other models. In the quasi-static range, this model underestimates the fracture energy experimentally obtained.

In the quasi-static range, the strain rate effect on the fracture behavior of SFRC is negligible. However, under impact loading rates, the strain rate effect is pronounced. In the impact range, the microinertial forces generated around the crack tip make fracture propagation difficult (Körmeling and Reinhardt 1987; Weerheijm and Forquin 2013; Zhang et al. 2014). In addition, the hooked-end steel fibers embedded in the concrete matrix support a higher load under the impact, and the pull-out energy is greater as well (Banthia and Trottier 1991).

Fig. 18 shows a comparison between the experimental results obtained on the DIF of fracture energy of SFRC and the results obtained by other researchers (Caverzan et al. 2012; Körmeling and Reinhardt 1987; Tran et al. 2016; Zhang et al. 2015) As shown, the fracture energy is more sensitive to the strain rate in the impact range compared to the quasi-static range. The fracture energy is mainly dependent on the fiber reinforcement mechanisms provided by fibers bridging the cracks. As already indicated, these fiber reinforcement mechanisms are significantly improved with increasing strain rate (Poveda et al. 2020; Tarifa et al. 2020); therefore, the fracture energy is one of the SFRC properties most benefited by the

Table 11. MAPE and MAD values for prediction of DIF_G by different models

	Quasi-static		Drop weight impact	
Reference	MAPE	MAD	MAPE	MAD
Proposed model	12.1	0.15	43.9	0.54
Zhang et al. (2014)	22.5	0.29	560.6	7.66
Körmeling and Reinhardt (1987)	55.4	0.65	191.7	2.35
Weerheijm and Forquin (2013)	19.52	0.25	851.72	11.61

strain rate loading conditions. There are two main aspects to be noted in this comparison. First, different fracture energy values are obtained at any strain rate. These differences increase with the strain rate value in the impact range and become more evident than in the range of quasi-static conditions. Second, the strain rates imposed under impact loading are generally lower than the ones adopted by other researchers, which means that the current work focuses on the lower strain rate range of impact. Considering these aspects, two empirical models are proposed to improve the prediction of results on fracture energy, taking into account both the strain rate and the testing approach effect, as reflected by Eqs. (13) and (14). Fig. 18 shows the comparison of DIF_G obtained from the experiments conducted and the ones obtained by other researchers.

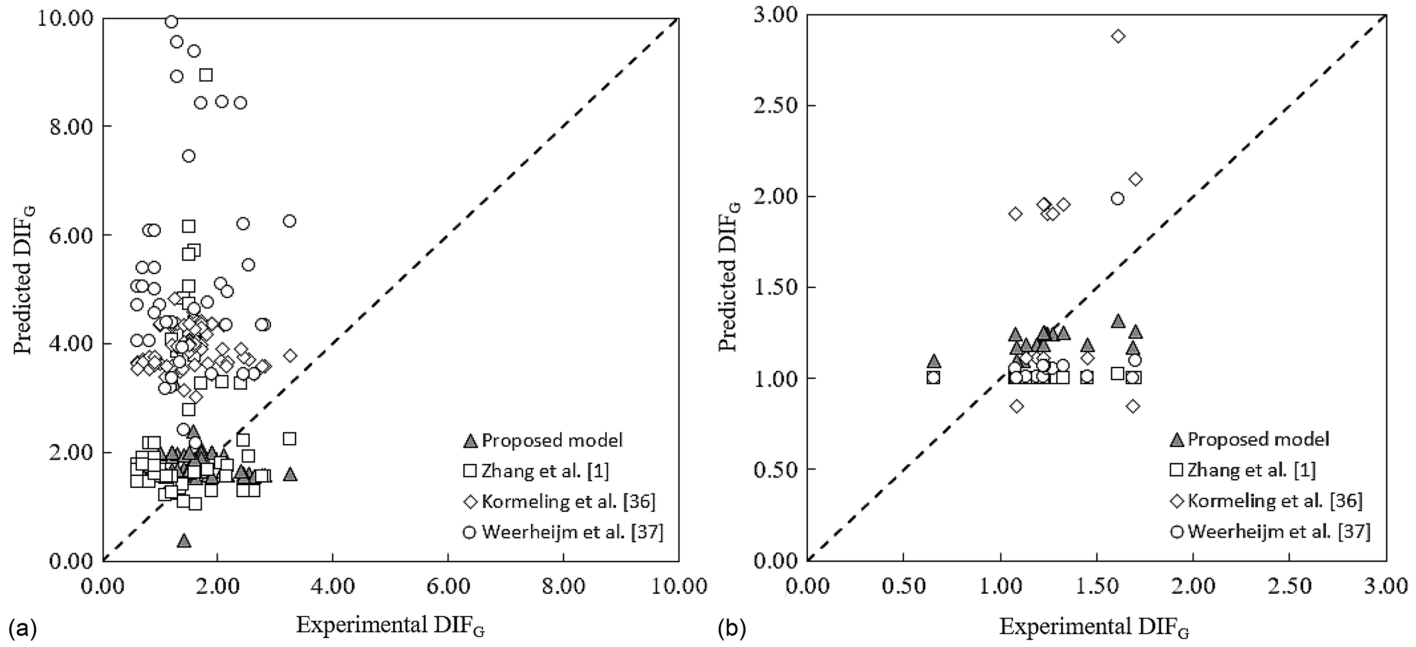

Fig. 19. Scatter in the prediction of DIFG: (a) quasi-static; and (b) drop weight impact.

MAD and MAPE values were calculated for each test type to evaluate the accuracy of the proposed models in predicting DIF$_G$, as presented in Table 11. When comparing the error values obtained, the prediction of DIF$_G$ seems to have improved with the proposed model. In the range of quasi-static, the model proposed by Körmeling et al. (1987) does not follow the trend of experimental results, resulting in MAD and MAPE values of 0.65 and 55.4%, respectively. This model presents the highest error for the DIF$_G$ in the quasi-static range. The proposed model has a MAD value of 0.15 and a MAPE value of 12.1%. Also, for drop weight impact tests, the experimental DIF$_G$ can be predicted more accurately with the proposed model, as shown in Table 11. Fig. 19 shows the scatter of results obtained when predicting DIF$_G$ using the models proposed by other researchers and the model proposed in the present study. The proposed empirical model can be used to estimate the DIF of SFRC material under high strain rate loadings. It should be noted that the proposed models are derived from test data that includes strain rates up to 50 s^{-1} for two different test approaches. Beyond this range and for other testing approaches, the proposed model is not validated.

Conclusions

The current research experimentally and analytically investigated the strain rate effect on the flexural behavior of steel fiber-reinforced concrete (SFRC) in both quasi-static and impact ranges. The study also investigated the effect of inertial force in the flexural impact loading of hooked-end SFRC and its relationship with the maximum acceleration measured at the midspan of the specimens. The conclusions drawn from the results and observations of this study are as follows:

1. The maximum acceleration at the midspan of the specimens increases with the strain rate. Consequently, the inertia force also increases. However, the ratio of inertia to impact load is approximately constant (average of 0.6) in the strain rate range between 1 and 20 s^{-1} (range of impact). This means that this ratio is not substantially rate-sensitive in the range of strain rates studied.
2. The flexural tensile strength and fracture energy of SFRC exhibit an increase with an increase in the strain rate, with a more significant effect observed in the impact range compared to the quasi-static range.
3. At the highest strain rate tested, the maximum DIF values achieved for the flexural tensile strength and fracture energy were 6.84 and 3.24, respectively. These maximum DIF values indicate that the mechanical properties of SFRC can be significantly affected by the strain rate.
4. In both quasi-static and impact loadings, the dominant failure mechanism of hooked-end fibers is pull-out. However, as the strain rate increases, the straightening of the hooked ends of the fiber becomes more apparent.
5. Under quasi-static loading, for increasing strain rates, the load decay observed in the post-peak phase of the load-CMOD responses tended to be more abrupt. This may be attributed to more brittle behavior of the specimens under higher loading rates.
6. In addition to the strain rate, the influence of the testing approach was considered to derive the proposed models. In this study, two different models were established for predicting flexural tensile strength and fracture energy of SFRC at different strain rates: one model in the range of quasi-static and another in the range of impact, corresponding to the drop weight impact test.
7. The flexural tensile strength and fracture energy DIF models proposed were able to describe the experimental DIF values of SFRC obtained more accurately than the other models considered.

The research's limitations include using only one volume fraction of steel fiber, limiting the fiber shape to hooked-end steel, and a narrow range of strain rates during impact testing. These factors may not fully represent SFRC's flexural behavior under different conditions.

Appendix. Previously Proposed Empirical Models for Dynamic Increase Factor

Parameter	Reference	Model
DIF of tensile strength	CEB-FIP Design Code (CEB-FIP 1990)	$\mathrm{DIF}_{f_{ct,\mathrm{direct}}} = \begin{cases} \left(\frac{\dot{\varepsilon}_t}{\dot{\varepsilon}_{ts}}\right)^{1.016\alpha}, & \dot{\varepsilon}_t \le 30\ \mathrm{s}^{-1} \\ \gamma\left(\frac{\dot{\varepsilon}_t}{\dot{\varepsilon}_{ts}}\right)^{\frac{1}{3}}, & \dot{\varepsilon}_t > 30\ \mathrm{s}^{-1} \end{cases}$ $\alpha = (10 + 0.6f_c)^{-1}, \log(\gamma) = 7.11\alpha - 2.33, \dot{\varepsilon}_{ts} = 3 \times 10^{-6}\ \mathrm{s}^{-1}$
	CEB-FIP Model Code (CEB-FIP 2010)	$\mathrm{DIF}_{f_{ct,\mathrm{direct}}} = \begin{cases} \left(\frac{\dot{\varepsilon}_t}{\dot{\varepsilon}_{ts}}\right)^{0.0018}, & \dot{\varepsilon}_t \le 10\ \mathrm{s}^{-1} \\ 0.0062\left(\frac{\dot{\varepsilon}_t}{\dot{\varepsilon}_{ts}}\right)^{\frac{1}{3}}, & \dot{\varepsilon}_t > 10\,\mathrm{s}^{-1} \end{cases}$, $\dot{\varepsilon}_{ts} = 1 \times 10^{-6}\ \mathrm{s}^{-1}$
	Malvar and Ross (1998)	$\mathrm{DIF}_{f_{ct,SHPB}} = \begin{cases} \left(\frac{\dot{\varepsilon}_t}{\dot{\varepsilon}_{ts}}\right)^{\alpha}, & \dot{\varepsilon}_t \le 1\ \mathrm{s}^{-1} \\ \gamma\left(\frac{\dot{\varepsilon}_t}{\dot{\varepsilon}_{ts}}\right)^{\frac{1}{3}}, & \dot{\varepsilon}_t > 1\ \mathrm{s}^{-1} \end{cases}$ $\alpha = (1 + 0.8f_c)^{-1}, \log(\gamma) = 6\alpha - 2, \dot{\varepsilon}_{ts} = 1 \times 10^{-6}\ \mathrm{s}^{-1}$
	Tedesco and Ross (1998)	$\mathrm{DIF}_{f_{ct,SHPB}} = \begin{cases} 0.1425(\log \dot{\varepsilon}_c) + 1.833, & \dot{\varepsilon}_t \le 2.32\ \mathrm{s}^{-1} \\ 2.9290(\log \dot{\varepsilon}_c) + 0.814, & \dot{\varepsilon}_t > 2.32\ \mathrm{s}^{-1} \end{cases}$
	Fujikake et al. (2006)	$\mathrm{DIF}_{f_{ct,\mathrm{direct}}} = \left(\frac{\dot{\varepsilon}_t}{\dot{\varepsilon}_{ts}}\right)^{0.0013[\log(\frac{\dot{\varepsilon}_t}{\dot{\varepsilon}_{ts}})]^{1.95}}$, $\dot{\varepsilon}_{ts} = 1 \times 10^{-6}\ \mathrm{s}^{-1}$
	Tran and Kim (2013)	$\mathrm{DIF}_{f_{ct,\mathrm{direct}}} = \begin{cases} \left(\frac{\dot{\varepsilon}_t}{\dot{\varepsilon}_{ts}}\right)^{h\alpha}, & \dot{\varepsilon}_t \le 1\ \mathrm{s}^{-1} \\ \gamma\left(\frac{\dot{\varepsilon}_t}{\dot{\varepsilon}_{ts}}\right)^{\frac{k}{3}}, & \dot{\varepsilon}_t > 1\ \mathrm{s}^{-1} \end{cases}$ $\alpha = (1 + 0.6f_c)^{-1}, \log(\gamma) = 6h\alpha - 2, \dot{\varepsilon}_{ts} = 1 \times 10^{-6}\ \mathrm{s}^{-1}$ $h = k = 1$, Hookedend fiber $h = 1.3, k = 0.8$, Twisted fiber
DIF of fracture energy	Körmeling and Reinhardt (1987)	$\mathrm{DIF}_G = 1.117 + 0.34 \ln(\dot{\delta}_t)$
	Weerheijm and Forquin (2013)	$\mathrm{DIF}_G = \begin{cases} 1 + \dot{\varepsilon}_t, & \dot{\varepsilon}_t \le 1\ \mathrm{s}^{-1} \\ 1.66 + 0.34\dot{\varepsilon}_t, & \dot{\varepsilon}_t > 1\ \mathrm{s}^{-1} \end{cases}$
	Zhang et al. (2014)	$\mathrm{DIF}_G = 1 + (7.6 \times 10^{-6})(\dot{\delta}_t)^{1.54}$

Note: $\dot{\varepsilon}_t$ is the tensile strain rate and $\dot{\varepsilon}_{ts}$ is the reference tensile strain rate corresponding to static loading. f_c is the compressive strength. $\dot{\delta}_t$ is the midspan deflection rate.

Data Availability Statement

All data, models, and code generated or used during the study appear in the published article.

Acknowledgments

The first author gratefully acknowledges the financial support of FCT for the Ph.D. Grant SFRH/BD/149246/2019. The study reported in this paper is part of the project "FemWebAI - Integrated approach for reliable and advanced analysis and design of sustainable construction systems in fiber-reinforced concrete, with reference PTDC/ECI-EST/6300/2020, supported by the Portuguese Science Foundation (FCT).

References

Abaza, O. A., and Z. S. Hussein. 2016. "Flexural behavior of steel fiber-reinforced rubberized concrete." *J. Mater. Civ. Eng.* 28 (1): 04015076. https://doi.org/10.1061/(ASCE)MT.1943-5533.0001334.

ACI (American Concrete Institute). 1996. *State-of-the-art report on fiber reinforced concrete*. ACI Committee 544. Farmington Hills, MI: ACI.
ACI (American Concrete Institute). 2017. *Report on measuring mechanical properties of hardened fiber reinforced concrete*. ACI Committee 544. Farmington Hills, MI: ACI.
Akcay, B., and M. A. Tasdemir. 2012. "Mechanical behaviour and fibre dispersion of hybrid steel fibre reinforced self-compacting concrete." *Constr. Build. Mater.* 28 (1): 287–293. https://doi.org/10.1016/j.conbuildmat.2011.08.044.
Bakhshi, M., I. B. Valente, H. Ramezansefat, J. A. Barros, E. N. Pereira, and N. R. Peixinho. 2023. "Experimental and analytical study of the high-strain-rate compressive behavior of SFRC." *Mech. Adv. Mater. Struct.* 1–24. https://doi.org/10.1080/15376494.2023.2199420.
Bakhshi, M., I. B. Valente, H. Ramezansefat, J. A. O. Barros, E. N. B. Pereira, and N. R. M. Peixinho. 2021. "Experimental investigation of the effect of high strain rate loading on the flexural behaviour of the steel fibre-reinforced concrete." In *Proc., fib Symp.*, 604–613. Braga, Portugal: Univ. of Minho.
Banthia, N., and S. Mindess. 1996. "Impact resistance of steel fiber reinforced concrete." *Mater. J.* 93 (5): 472–479. https://doi.org/10.14359/9852.
Banthia, N., S. Mindess, A. Bentur, and M. Pigeon. 1989. "Impact testing of concrete using a drop-weight impact machine." *Exp. Mech.* 29 (1): 63–69. https://doi.org/10.1007/BF02327783.
Banthia, N., and J.-F. Trottier. 1991. "Deformed steel fiber—Cementitious matrix bond under impact." *Cem. Concr. Res.* 21 (1): 158–168. https://doi.org/10.1016/0008-8846(91)90042-G.
Banthia, N., C. Yan, and K. Sakai. 1998. "Impact resistance of fiber reinforced concrete at subnorma temperatures." *Cem. Concr. Compos.* 20 (5): 393–404. https://doi.org/10.1016/S0958-9465(98)00015-8.
Banthia, N. P. 1987. *Impact resistance of concrete*. Vancouver, BC, Canada: Univ. of British Columbia.
Banthia, N. P., S. Mindess, and A. Bentur. 1987. "Impact behaviour of concrete beams." *Mater. Struct.* 20 (4): 293–302. https://doi.org/10.1007/BF02485926.
Barros, J. A. O., I. G. Costa, C. M. V. Frazão, T. D. S. Valente, L. A. P. Lourenço, and F. J. S. A. Melo. 2022a. "Innovative prefabricated lightweight slab system of high structural performance." *Eng. Struct.* 259 (Jun): 114146. https://doi.org/10.1016/j.engstruct.2022.114146.
Barros, J. A. O., and J. A. Figueiras. 1999. "Flexural behavior of SFRC: Testing and modeling." *J. Mater. Civ. Eng.* 11 (4): 331–339. https://doi.org/10.1061/(ASCE)0899-1561(1999)11:4(331).
Barros, J. A. O., T. D. S. Valente, I. G. Costa, and F. J. S. A. Melo. 2022b. "Integrating hybrid reinforced concrete technology and advanced FEM-based numerical modelling for crack control in long concrete foundations without joints." In *Proc., RILEM Int. Conf. on Numerical Modeling Strategies for Sustainable Concrete Structures*, 33–46. New York: Springer.
Bentur, A., and S. Mindess. 2006. *Fibre reinforced cementitious composites*. Boca Raton, FL: CRC Press.
Bhowmik, S., and S. Ray. 2019. "An experimental approach for characterization of fracture process zone in concrete." *Eng. Fract. Mech.* 211 (Jun): 401–419. https://doi.org/10.1016/j.engfracmech.2019.02.026.
British Standard Euro Norm. 2000. *Cement. Composition, specifications and conformity criteria for common cements*. BS EN 197-1. London: British Standards Institute.
British Standard Euro Norm. 2012. *Fly ash for concrete—Definition, specifications and conformity criteria*. BS EN 450-1. London: British Standards Institute.
Caverzan, A., E. Cadoni, and M. Di Prisco. 2012. "Tensile behaviour of high performance fibre-reinforced cementitious composites at high strain rates." *Int. J. Impact Eng.* 45 (Feb): 28–38. https://doi.org/10.1016/j.ijimpeng.2012.01.006.
CEB-FIP (Comité européen du béton-Fédération Internationale de la Précontrainte). 1990. *Design code 1990*, 51–59. London: Thomas Telford.
CEB-FIP (Comité européen du béton-Fédération Internationale de la Précontrainte). 2010. *Model code 2010*. London: Thomas Telford.
Fujikake, K., T. Senga, N. Ueda, T. Ohno, and M. Katagiri. 2006. "Effects of strain rate on tensile behavior of reactive powder concrete." *J. Adv. Concr. Technol.* 4 (1): 79–84. https://doi.org/10.3151/jact.4.79.
Gao, X., T. C. K. Molyneaux, I. Patnaikuni, and S. M. S. Rahman. 2020. "Dynamic properties of fibre reinforced and plain ultra high performance concretes." In *Proc., Int. Conf. Innovation Good Practice and Research in Engineering Education*, 569–573. Boca Raton, FL: CRC Press.
Gopalaratnam, V. S., and S. P. Shah. 1986. "Properties of steel fiber reinforced concrete subjected to impact loading." *ACI J.* 83 (1): 117–126.
Jin, L., R. Zhang, G. Dou, J. Xu, and X. Du. 2018. "Experimental and numerical study of reinforced concrete beams with steel fibers subjected to impact loading." *Int. J. Damage Mech.* 27 (7): 1058–1083. https://doi.org/10.1177/1056789517721616.
Körmeling, H. A., and H. W. Reinhardt. 1987. "Strain rate effects on steel fibre concrete in uniaxial tension." *Int. J. Cem. Compos. Lightweight Concr.* 9 (4): 197–204. https://doi.org/10.1016/0262-5075(87)90002-9.
Lok, T. S., X. B. Li, D. Liu, and P. J. Zhao. 2002. "Testing and response of large diameter brittle materials subjected to high strain rate." *J. Mater. Civ. Eng.* 14 (3): 262–269. https://doi.org/10.1061/(ASCE)0899-1561(2002)14:3(262).
Lok, T. S., and P. J. Zhao. 2004. "Impact response of steel fiber-reinforced concrete using a split Hopkinson pressure bar." *J. Mater. Civ. Eng.* 16 (1): 54–59. https://doi.org/10.1061/(ASCE)0899-1561(2004)16:1(54).
Lok, T. S., P. J. Zhao, and G. Lu. 2003. "Using the split Hopkinson pressure bar to investigate the dynamic behaviour of SFRC." *Mag. Concr. Res.* 55 (2): 183–191. https://doi.org/10.1680/macr.2003.55.2.183.
Malvar, L. J., and C. A. Ross. 1998. "Review of strain rate effects for concrete in tension." *ACI Mater. J.* 95 (Jun): 735–739. https://doi.org/10.14359/418.
Millard, S. G., T. C. K. Molyneaux, S. J. Barnett, and X. Gao. 2010. "Dynamic enhancement of blast-resistant ultra high performance fibre-reinforced concrete under flexural and shear loading." *Int. J. Impact Eng.* 37 (4): 405–413. https://doi.org/10.1016/j.ijimpeng.2009.09.004.
Mujalli, M. A., S. Dirar, E. Mushtaha, A. Hussien, and A. Maksoud. 2022. "Evaluation of the tensile characteristics and bond behaviour of steel fibre-reinforced concrete: An overview." *Fibers* 10 (12): 104. https://doi.org/10.3390/fib10120104.
Naaman, A. E., and V. S. Gopalaratnam. 1983. "Impact properties of steel fibre reinforced concrete in bending." *Int. J. Cem. Compos. Lightweight Concr.* 5 (4): 225–233. https://doi.org/10.1016/0262-5075(83)90064-7.
Nyström, U., and K. Gylltoft. 2009. "Numerical studies of the combined effects of blast and fragment loading." *Int. J. Impact Eng.* 36 (8): 995–1005. https://doi.org/10.1016/j.ijimpeng.2009.02.008.
Othman, H., and H. Marzouk. 2016. "An experimental investigation on the effect of steel reinforcement on impact response of reinforced concrete plates." *Int. J. Impact Eng.* 88 (Apr): 12–21. https://doi.org/10.1016/j.ijimpeng.2015.08.015.
Othman, H., H. Marzouk, and M. Sherif. 2019. "Effects of variations in compressive strength and fibre content on dynamic properties of ultra-high performance fibre-reinforced concrete." *Constr. Build. Mater.* 195 (Jun): 547–556. https://doi.org/10.1016/j.conbuildmat.2018.11.093.
Ozden, G., and C. T. Akdag. 2009. "Lateral load response of steel fiber reinforced concrete model piles in cohesionless soil." *Constr. Build. Mater.* 23 (2): 785–794. https://doi.org/10.1016/j.conbuildmat.2008.03.001.
Park, J., S. Yoon, T.-H. Kwon, and K. Park. 2017. "Assessment of speckle-pattern quality in digital image correlation based on gray intensity and speckle morphology." *Opt. Lasers Eng.* 91 (Apr): 62–72. https://doi.org/10.1016/j.optlaseng.2016.11.001.
Poveda, E., R. C. Yu, M. Tarifa, G. Ruiz, V. M. C. F. Cunha, and J. A. O. Barros. 2020. "Rate effect in inclined fibre pull-out for smooth and hooked-end fibres: A numerical study." *Int. J. Fract.* 223 (1): 135–149. https://doi.org/10.1007/s10704-019-00404-7.
Rahmani, T., B. Kiani, M. Shekarchi, and A. Safari. 2012. "Statistical and experimental analysis on the behavior of fiber reinforced concretes subjected to drop weight test." *Constr. Build. Mater.* 37 (Aug): 360–369. https://doi.org/10.1016/j.conbuildmat.2012.07.068.
Rasheed, M. A., and S. S. Prakash. 2018. "Behavior of hybrid-synthetic fiber reinforced cellular lightweight concrete under uniaxial

tension–Experimental and analytical studies." *Constr. Build. Mater.* 162 (Jun): 857–870. https://doi.org/10.1016/j.conbuildmat.2017.12.095.
RILEM 50-FMC Committee. 1985. "Determination of the fracture energy of mortar and concrete by means of three-point bend tests on notched beams." *Mater. Struct.* 18 (106): 285–290.
Sorelli, L. G., A. Meda, and G. A. Plizzari. 2006. "Steel fiber concrete slabs on ground: A structural matter." *ACI Mater. J.* 103 (4): 551. https://doi.org/10.14359/16431.
Suaris, W., and S. P. Shah. 1982. "Strain-rate effects in fibre-reinforced concrete subjected to impact and impulsive loading." *Composites* 13 (2): 153–159. https://doi.org/10.1016/0010-4361(82)90052-0.
Suaris, W., and S. P. Shah. 1983. "Properties of concrete subjected to impact." *J. Struct. Eng.* 109 (7): 1727–1741. https://doi.org/10.1061/(ASCE)0733-9445(1983)109:7(1727).
Taheri, M., J. A. O. Barros, and H. Salehian. 2020. "Integrated approach for the prediction of crack width and spacing in flexural FRC members with hybrid reinforcement." *Eng. Struct.* 209 (Aug): 110208. https://doi.org/10.1016/j.engstruct.2020.110208.
Tarifa, M., E. Poveda, V. M. C. F. Cunha, and J. A. O. Barros. 2020. "Effect of the displacement rate and inclination angle in steel fiber pullout tests." *Int. J. Fract.* 223 (1): 109–122. https://doi.org/10.1007/s10704-019-00398-2.
Tedesco, J. W., and C. A. Ross. 1998. "Strain-rate-dependent constitutive equations for concrete." *J. Pressure Vessel Technol.* 120 (4): 398–405. https://doi.org/10.1115/1.2842350.
Tlemat, H., K. Pilakoutas, and K. Neocleous. 2003. "Flexural toughness of SFRC made with fibres extracted from tyres." In *Proc., Int. Symp. Advances in Recycling & Waste Management*, 365–374. London: Thomas Telford.
Tran, N. T., T. K. Tran, J. K. Jeon, J. K. Park, and D. J. Kim. 2016. "Fracture energy of ultra-high-performance fiber-reinforced concrete at high strain rates." *Cem. Concr. Res.* 79 (Feb): 169–184. https://doi.org/10.1016/j.cemconres.2015.09.011.
Tran, T. K., and D. J. Kim. 2013. "Investigating direct tensile behavior of high performance fiber reinforced cementitious composites at high strain rates." *Cem. Concr. Res.* 50 (Jan): 62–73. https://doi.org/10.1016/j.cemconres.2013.03.018.
Ulzurrun, G., and C. Zanuy. 2017. "Flexural response of SFRC under impact loading." *Constr. Build. Mater.* 134 (Aug): 397–411. https://doi.org/10.1016/j.conbuildmat.2016.12.138.
Vandewalle, L., et al. 2022. "Test and design methods for steel fibre reinforced concrete—Final recommendation." *Mater. Struct.* 35 (253): 579–582.
Wang, S., M.-H. Zhang, and S. T. Quek. 2011. "Effect of high strain rate loading on compressive behaviour of fibre-reinforced high-strength concrete." *Mag. Concr. Res.* 63 (11): 813–827. https://doi.org/10.1680/macr.2011.63.11.813.
Weerheijm, J., and P. Forquin. 2013. "Response mechanisms of concrete under impulsive tensile loading." In *Understanding the tensile properties of concrete*, 181–217. Amsterdam, Netherlands: Elsevier.
Wu, H., Q. Fang, J. Gong, J. Z. Liu, J. H. Zhang, and Z. M. Gong. 2015. "Projectile impact resistance of corundum aggregated UHP-SFRC." *Int. J. Impact Eng.* 84 (Jun): 38–53. https://doi.org/10.1016/j.ijimpeng.2015.05.007.
Xu, S., C. Wu, Z. Liu, K. Han, Y. Su, J. Zhao, and J. Li. 2017. "Experimental investigation of seismic behavior of ultra-high performance steel fiber reinforced concrete columns." *Eng. Struct.* 152 (Feb): 129–148. https://doi.org/10.1016/j.engstruct.2017.09.007.
Yoo, D.-Y., and N. Banthia. 2017. "Size-dependent impact resistance of ultra-high-performance fiber-reinforced concrete beams." *Constr. Build. Mater.* 142 (May): 363–375. https://doi.org/10.1016/j.conbuildmat.2017.03.080.
Yoo, D.-Y., and N. Banthia. 2019. "Impact resistance of fiber-reinforced concrete—A review." *Cem. Concr. Compos.* 104 (Aug): 103389. https://doi.org/10.1016/j.cemconcomp.2019.103389.
Yoo, D.-Y., S.-T. Kang, and Y.-S. Yoon. 2016. "Enhancing the flexural performance of ultra-high-performance concrete using long steel fibers." *Compos. Struct.* 147 (Feb): 220–230. https://doi.org/10.1016/j.compstruct.2016.03.032.
Yoo, D.-Y., Y.-S. Yoon, and N. Banthia. 2015. "Flexural response of steel-fiber-reinforced concrete beams: Effects of strength, fiber content, and strain-rate." *Cem. Concr. Compos.* 64 (Jan): 84–92. https://doi.org/10.1016/j.cemconcomp.2015.10.001.
Zanuy, C., and G. S. D. Ulzurrún. 2017. "Rate effects of fiber-reinforced concrete specimens in impact regime." *Procedia Eng.* 193 (Feb): 501–508. https://doi.org/10.1016/j.proeng.2017.06.243.
Zhang, X., G. Ruiz, M. Tafira, and D. A. Cendon. 2015. "Loading rate effect on the fracture behaviour of three different steel fiber-reinforced concretes." In *Proc., 9th Int. Conf. FraMCoS-9*, edited by V. Sauoma, J. Bolander, and E. Landis. Los Angeles: Univ. of California.
Zhang, X., G. Ruiz, M. Tarifa, D. Cendón, F. Gálvez, and W. H. Alhazmi. 2017. "Dynamic fracture behavior of steel fiber reinforced self-compacting concretes (SFRSCCs)." *Materials* 10 (11): 1270. https://doi.org/10.3390/ma10111270.
Zhang, X. X., A. M. Abd Elazim, G. Ruiz, and R. C. Yu. 2014. "Fracture behaviour of steel fibre-reinforced concrete at a wide range of loading rates." *Int. J. Impact Eng.* 71 (Jan): 89–96. https://doi.org/10.1016/j.ijimpeng.2014.04.009.
Zhang, X. X., G. Ruiz, R. C. Yu, and M. Tarifa. 2009. "Fracture behaviour of high-strength concrete at a wide range of loading rates." *Int. J. Impact Eng.* 36 (10–11): 1204–1209. https://doi.org/10.1016/j.ijimpeng.2009.04.007.